Iron-Based Dye-Sensitized Solar Cells

From Theory to Working Solar Cells

DIVISION OF CHEMICAL PHYSICS | FACULTY OF ENGINEERING | LUND UNIVERSITY
LINNEA LINDH | MASTER'S THESIS 2019

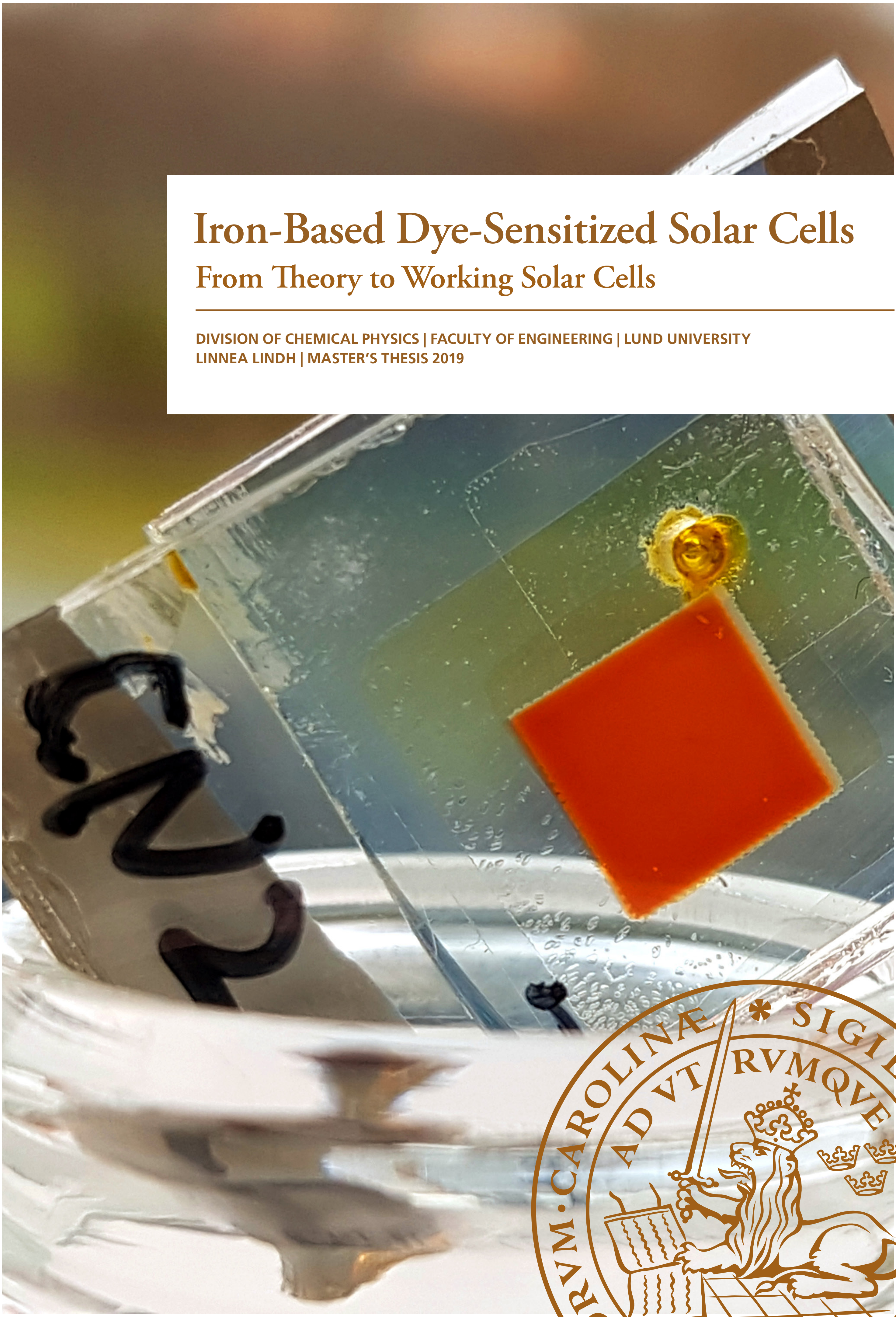

1 Abstract

In the hunt for fossile-free energy-harvesting techniques, solar cells constitute one of the most promising techniques. Today, silicon-based solar cells are the dominant technique on the market but even the silicon solar cell has limitations which means that there is a motivation for developing new solutions. One of those techniques is the dye-sensitized solar cell. Just as in photosynthesis, the solar cell contains a dye molecule that when absorbing the light from the sun can separate an electron from an electron hole. The electron is injected into titania and from there extracted as current. In this Master's thesis, two new dye molecules called FeCAB26 and FeCABCN2 have been investigated by spectroscopic methods (absorption spectroscopy, emission spectroscopy and transient absorption spectroscopy), quantum-chemical calculations and electrical measurements with the purpose to investigate the potential for usage as sensitizers in dye-sensitized solar cells. The molecules are iron-carbene-complexes, synthesized by colleges at Lund University, which are at the frontier of this research field since many traditionally used sensitizers have been ruthenium-complexes.

Both molecules were able to sensitize films of titania and absorb light in the visible part of the spectrum. Quantum-chemical calculations indicated that the molecules did excite an electron from metal-centred orbitals to ligand-centred orbitals upon absorption of light. The molecules did also inject electrons into titania via the excited metal-to-ligand charge transfer state. The excited states had lifetimes of 21 ps and 36 ps for the different molecules. When the dye molecules were used as sensitizers in solar cells, a photocurrent was measured upon illumination in a solar simulator for the molecule FeCABCN2. Without having optimized the fabrication process, the efficiency of the best solar cell was 0.13 %. This shows a proof of concept that FeCABCN2 could work as a sensitizer in DSSCs. The optical characterization of both molecules will contribute to the development of iron-carbene-complexes as dye molecules to be used for applications in a broader context than just solar cells.

2 Sammanfattning

I jakten på förnyelsebara energikällor är solceller en av de mest lovande teknikerna. Idag dominerar kisel-solcellen marknaden men även den har begränsningar och därför är det motiverat att utveckla andra sorters solceller. En solcellsteknik på utvecklingsstadiet som försöker efterlikna fotosyntesen är Grätzelsolcellen. Precis som i fotosyntesen är det en färgämnesmolekyl i solcellen som ska absorbera solens ljus och separera en elektron från ett elektronhål genom att elektronen skickas från färgämnesmolekylen till en titandioxid-elektrod och därifrån extraheras som elektrisk ström. I detta masterarbete har två nya färgämnesmolekyler kallade FeCAb26 och FeCAbCN2 undersökts genom en rad spektroskopiska (absorptionsspektroskopi, emissionsspektroskopi, tidsupplöst laserspektroskopi), beräkningskemiska och elektriska mätmetoder med målet att bestämma deras fotofysiska egenskaper och bedöma dugligheten för bruk i Grätzelsolceller. Färgämnes-
molekylerna är båda järnkarben-komplex, syntetiserade av kollegor vid Lunds universitet, vilka är i framkanten av forskningen inom detta fält där många metallbaserade färgämnesmolekyler annars varit rutenium-komplex.

Båda molekylerna visade sig fästa till titandioxidytor och absorbera ljus i det synliga våglängdsområdet. De kvantkemiska beräkningarna indikerade att färgämnesmolekylerna vid absorption av ljus exciterade en elektron i en metall-centrerad orbital till ligand-centrerade orbitaler. De exciterade tillstånden hade livstider på 21 ps respektive 36 ps. Färgämnesmolekylerna visade sig även injicera elektroner i titandioxiden vid belysning. När färgämnesmolekylerna införlivades i solceller, så kunde en elektrisk ström mätas under belysning i solsimulator för FeCABCN2. Utan att ha optimerat tillverkningsprocessen var effekten för de bästa solcellerna med FeCABCN2 runt 0,13 %. Som ett första steg visar detta att FeCAbCN2-färgämnet principiellt sett fungerar, även om fortsatt utveckling mot bättre solceller av denna typ kräver omfattande fortsatt forskning. Karaktäriseringen av båda molekylernas optiska egenskaper bidrar även till den fortsatta utvecklingen av järnkarben-komplex som färgämnesmolekyler mer generellt.

3 Acknowledgements

Firstly, I would like to thank the dynamics iron-carbene group at Chemical Physics and Theoretical Chemistry Lund University. You took me in without knowing what really to expect and were eager to make sure that I had fun, learned a lot and was considered a part of the group. Everyone in the group, regardless if they were supervisor or not, were eager to help me and I am truly greatful for that. My actual supervisors; Pavel Chábera and Petter Persson, deserve a huge thank you for all the support, discussions and fun during my thesis. A special thanks goes to my consultant Nils Rosemann who helped me a lot with labwork and often was my first-person-to-ask. I would also like to mention my spectroscopy expert Arkady Yartsev, my co-co-supervisor Alireza Honafar and my data analysis guru Jens Uhlig.

Finding a Master's thesis project that really suited me was far from easy, and I would like to thank everyone who agreed to discuss with me about my ideas and pointed me in the right direction. A special thank in this regard I would like to give Charlotta Nilsson who was always ready to listen to my hard decisions. I would like to thank Kenneth Wärnmark and the synthetic group at CAS Lund University who let me take part of their fantastic iron-carbenes and collaboration! A special thanks goes to Olga Gordivska and Om Prakash who synthesized the molecules investigated in this thesis. I would also like to thank the group of Gerrit Boschloo and the group of Marina Freitag at Physical Chemistry Uppsala University who made it possible for me to build actual solar cells and measure their characteristics. And of course thank you to the people who actually participated in fabricating the solar cells with me: Hao Fan, Olga Gordivska, Pavel Chábera and Hannes Michaels.

A big project is never possible without great support from family and friends. Thank you for never stopping to believe in me and being there for me in hard times as well as for listening to me talking about solar cells in good times. A special thanks to my grandfather who thought that if someone could do something, it was Linnea. And finally, thank you Robin. Thank you for all the technical support making it possible for me to write this thesis in LaTeX. Thank you for keeping me company while writing and revising texts. But most importantly, thank you for the endless amount of 24/7 love and personal support.

Contents

List of Figures

List of Tables

4 Abbreviations

DSSC - dye sensitized solar cell, also called Grätzel cell
TiO_2 - titanium dioxide, also called titania
M - metal
L - ligand
LUMO - lowest unoccupied molecular orbital
GS - ground state
MLCT - metal-to-ligand charge-transfer
MC - metal-centred
ISC - intersystem crossing
NHC - N-heterocyclic carbene
FWHM - full width half maxiumum
OD - optical density
PMT - photomultiplier tube
FF - front face
RA - right angle
TAS - transient absorption spectroscopy
OPA - optical parametric amplifier
WLC - white light continuum
TA - transient absorption
GSB - ground state bleach
SE - stimulated emission
ESA - excited state absorption
OC - open circuit
SC - short circuit
FF - fill factor
AM - air mass
MP - maximum power
IPCE - incident photon-to-current conversion efficiency
PIA - photon induced absorption
DFT - density functional theory
TD-DFT - time-dependent density functional theory
MeCN - acetonitrile
FTO - fluorine-doped tin oxide
EtOH - ethanol
PEDOT - poly(3,4-ethylenedioxythiophene)
TPAA - tris(p-anisyl)amine
HOMO - highest occupied molecular orbital

5 Introduction

5.1 Motivation

In a world where global warming is a real problem concerning all nations on Earth, the United Nations has set up a target within the Paris agreement in 2015 to not increase the average earth temperature by more than 2°C. To mitigate climate change, there needs to be a development of efficient fossil-free energy harvesting techniques.[1] Solar cells are thought to be one of the most promising technologies since more than 99 % of all the earth's near-surface renewable energy comes from the sun in the form of light. To be able to make a large-scale solar cell device, rare and expensive metals can not be a major part.[2] Hence, to invent a solar cell made of inexpensive, environmentally friendly compounds able to produce energy in large scale is one current research goal in the solar energy field.

5.2 Background

The most common solar cell on the market today is based on an internal electric field created in silicon that can, when it is irradiated by light, separate an electron from an electron hole and extract the photocurrent.[3] To fabricate such a solar cell, however, demands a series of high-temperature and very clean processes. Also, silicon has a fixed band gap making it non-trivial to change the absorption range.[4] If we instead look at how nature harvests the energy from the sun we can investigate plants and bacteria that perform photosynthesis. These organisms can also separate an electron and a hole when irradiated by sunlight, since they have certain metal-organic molecular light-harvesting complexes (dye molecules).[5]

A type of solar cell using dye molecules for light-harvesting is the Grätzel cell, or the dye-sensitized solar cell (DSSC).[6] These solar cells commonly use ruthenium-based dyes. Ruthenium is not ideal to be used in solar cells due to it being a rare metal.[2] In 2015 researchers at the Chemistry Department in Lund had a breakthrough where ruthenium was replaced by iron.[7] Different iron-nitrogen-heterocyclic-carbenes are now investigated as potential alternatives for an efficient dye molecule in DSSCs.[8][9] DSSCs with iron-based dyes could be an alternative to silicon solar cells that would be inexpensive, environmentally friendly and versatile.[7][9]

5.3 Research Target

The goal of this Master's thesis is to characterize the new iron-based dye molecules seen in Figure 5.1 and evaluate their potential for usage in DSSCs. The molecules have recently been synthesized in-house by the group of Kenneth Wärnmark at Lund University, and are part of a series of new iron-carbene-complexes to be used as sensitizers in DSSCs. The project aims to provide a comprehensive understanding of how the fundamental molecular properties influence key photoinduced electronic processes down to ultrafast (femtosecond – picosecond) processes, as well as to relate this to characterization of overall device performance.

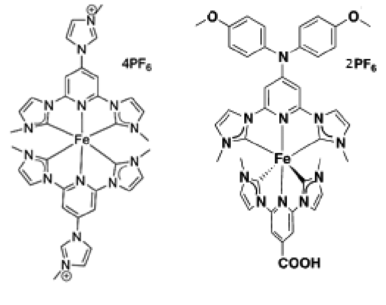

FeCAB26 **FeCABCN2**

Figure 5.1: Dye molecules developed for potential usage in DSSCs to be characterized in this Master's thesis, synthesized by Om Prakash and Olga Gordivska in the Wärnmark group.

FeCAB26 is the common name of bis[2,6-bis(3-methylimidazol-1-ylidene), 4-(3-methylimidazolium-1-yl) pyridine)]iron(II) tetrakis(hexafluorophosphate) which is a homoleptic N-heterocyclic iron-carbene-complex with imidazolium anchoring groups. FeCABCN2 is the common name of [(2,6-bis(3-methylimidazol-1-ylidene) pyridine-4-carboxylic acid)(2,6-bis(3-methylimidazol-1-ylidene)pyridine-4-bis-(4-methoxy-phenyl)-amine)] iron(II) bis hexafluorophosphate which is a heteroleptic N-heterocyclic iron-carbene-complex with one carboxylic anchoring group.

6 Scientific background

6.1 Dye-Sensitized Solar Cell

The first dye sensitized solar cell with appreciable efficiency was reported by Michael Grätzel and Brian O'Regan in 1991. The DSSC consists of a charge-transfer dye adsorbed on a film of TiO_2-nanoparticles, enclosed in a solution of a regeneration redox couple between two electrodes. The dye used was a ruthenium-complex, and the maximum achieved efficiency was almost 8 % in simulated solar light.[6] The difference from previous similar cells, was the ability to adsorb a lot more dye due to the nanostructured TiO_2. A scheme of a working DSSC can be seen in Figure 6.1.[2]

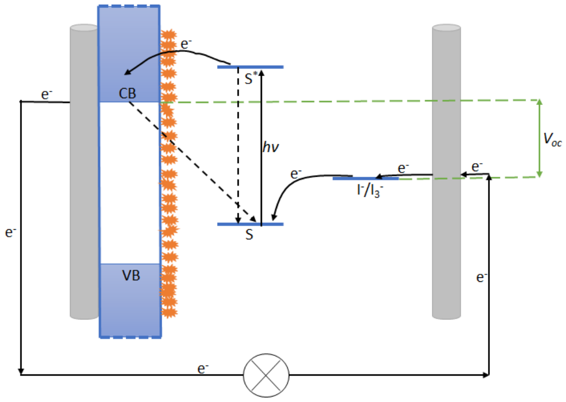

Figure 6.1: The dye sensitized solar cell working scheme. CB/VB are the conduction/valence band of the semiconductor. S (S*) is the (excited) sensitizer/dye. I^- / I_3^- is the regeneration redox couple. The silver coloured rods are the electrodes and the orange particles are the dye molecules (not to scale).

Light, of energy hν, excites an electron in the dye molecule (sensitizer), transferring the molecule from ground state (S) to its first excited state (S*), as seen in Figure 6.1. Excitation of the dye comprises the separation of an electron and an electron hole. The electron in S* ends up in an excited state higher in energy than the semiconductor (in all cases in this thesis TiO_2) conduction band, CB. Thus the electron can be injected into the TiO_2, but it can also go back to the ground state in a process called relaxation. The TiO_2 is connected to an electrode that allows the electron to move in a circuit to the counter electrode. Between the electrodes there is a redox mediator, I^-/I_3^- in Figure 6.1, that takes an electron from the electrode and gives it to the dye, thus regenerating it. The difference in voltage between the redox potential of the redox mediator and the conduction band edge (CB) of TiO_2 becomes the open circuit voltage of the solar cell (indicated by V_{oc} in Figure 6.1)[2][10]

Many parameters of the DSSC are important for its performance, such as the TiO_2 film, the dye, the electrode material, the redox mediator i.e. the electrolyte, etc. It is a non-trivial problem to scientists within the field to understand how different dyes will work together with different electrolytes. However, it is important that the electrolyte can regenerate the excited dye before charge recombination occurs. Charge recombination is the process where an injected electron goes back to the dye instead of going in the circuit, indicated by the yellow arrow in Figure 6.1. Thus, a good dye should have high injection quantum yield and slow charge recombination.[2][10]

6.2 MO-Theory

For transition metals oxidized two times becoming M^{2+}-ions (M=metal), the outermost s-electrons are lost. This leaves the outermost d-orbitals as the frontier orbitals of the ion. The five different d-orbitals are shown in Figure 6.2. For Fe^{2+}-ions it is the 3d-orbitals and for Ru^{2+}-ions, being one row down in the periodic system, it is the 4d-orbitals which have similar shapes but longer atomic radii compared to the 3d-orbitals. The d-orbitals for an isolated ion all have the same energy, i.e. they are degenerate.[11][12]

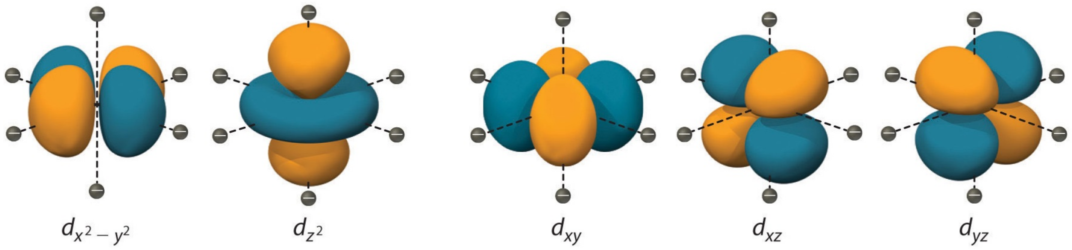

Figure 6.2: The d-orbitals, which are the frontier orbitals for an Fe^{2+}-ion. Image taken from https://chem.libretexts.org/.

In the scope of this thesis, organic ligands bind to the M^{2+}-ion and interact with the outermost d-orbitals in a partly ionic, partly covalent fashion. The ionic contribution consists of electrostatic attraction between the positive metal and the partly negative ligands. The covalent contribution consists of orbital overlap and mixing between the metal and ligands, see Figure 6.3 c. The metal-complexes in this thesis form octahedral bistridentate complexes $M^{2+}L_6$ (L=ligand), meaning that there are two ligands per metal ion coordinating at three positions on the metal each (see Figure 5.1). All metal-ligand coordination occurs on the axes seen in Figure 6.2 (ideal case), which means that the two d-orbitals d_{z^2} and $d_{x^2-y^2}$ that have lobes pointing along at least one axis will face towards the ligands.

Since all d-orbitals before bonding contain electrons, and the ligands are partly negatively charged, the d-orbitals facing ligands upon bonding will be higher in energy than the rest. This results in a splitting of the d-orbitals upon bonding to ligands, forming the two groups: t_{2g} consisting of d_{xy}, d_{yz} and d_{xz} being lower in energy, and e_g consisting of d_{z^2} and $d_{x^2-y^2}$ being higher in energy, see Figure 6.3 a. Stronger negative charge on the ligands gives a stronger ligand field, and results in a larger splitting of the d-orbitals. In this thesis, all ligands have relatively high ligand field strength. This results in an electron configuration as shown in Figure 6.3 b.[12]

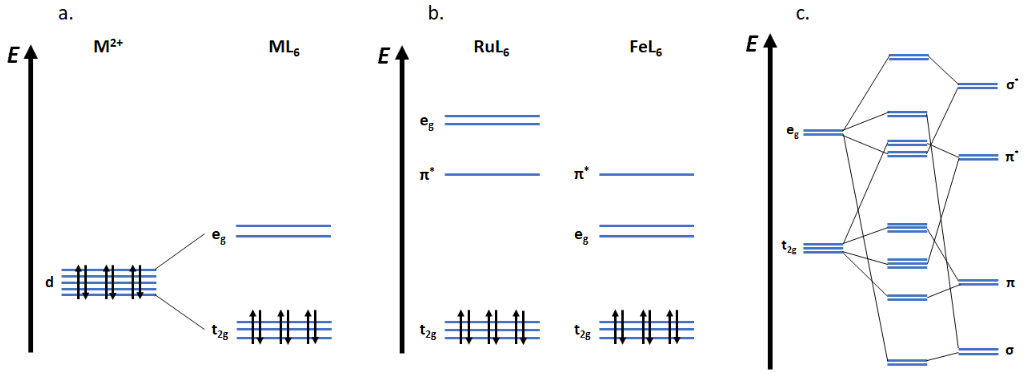

Figure 6.3: a, splitting of the M^{2+} d-orbitals upon bonding with with ligands. b, comparison of relevant orbital energy positions for RuL_6 and for FeL_6. c, mixing of orbitals between Fe and the ligands in an FeL_6-complex. The energy levels in c are not drawn to scale with a and b. Also the energy levels of the orbitals are just a schematic and the real picture looks different. The schematic diagram does not show electrons populating the orbitals.

Figure 6.3 shows a schematic of the relevant orbitals for the $M^{2+}L_6$-system as a function of energy. The horizontal lines indicate the energy of each orbital. π^* is the LUMO of the ligands used in this thesis and is effectively a couple of near-degenerate π^*-orbitals (not one or two as in Figure 6.3). The other ligand orbitals in Figure 6.3 c (σ, π, $\sigma*$) are also a number of near-degenerate orbitals and not two as in the schematic. Figure 6.3 b compares the important orbital energy levels for typical RuL_6- and FeL_6-complexes. The main difference is the position of the e_g-orbitals, for RuL_6 they are above the π^*-orbitals and for FeL_6 they are below the π^*-orbitals.[13][2]

Transition rules for electronic dipole transitions (promotion of an electron when light is absorbed) in this system proclaims that the spin of the electron must not change.[14] The lowest in energy theoretically allowed transition involves promotion of an electron from a t_{2g}-orbital to a π^*-orbital while keeping the spin. This excitation shifts an electron (i.e. charge) from a metal-centred orbital to a ligand-centred orbital, and is thus called an metal-to-ligand charge-transfer (MLCT) transition.[15] The new configuration, shown in Figure 6.4, is called ^{1}MLCT since the two unpaired electrons form a singlet.[15][16]

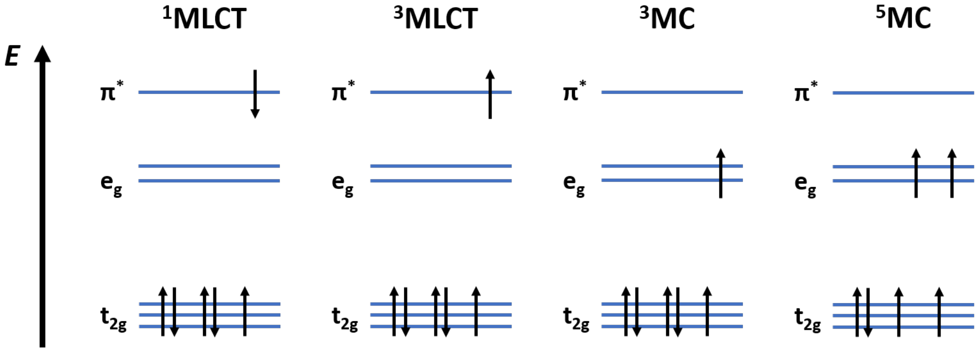

Figure 6.4: Comparison of relevant configurations for a $M^{2+}L_6$-system. Since the exact position of the e_g-orbitals change depending on the metal, a system similar to $Fe^{2+}L_6$ is shown here.

Another possible configuration would be to have the electrons in the same orbitals as for ^{1}MLCT, but to have the unpaired electrons parallel. This configuration, also seen in Figure 6.4 is called ^{3}MLCT since the two unpaired electrons form a triplet.[15][16] This lowers the energy of the system due to Hund's rule.[12][11]

If one would instead promote one electron from a t_{2g}-orbital to an e_g-orbital (not allowed transition) and pair them according to Hund's rule, the configuration would look as in Figure 6.4 (^{3}MC). In this case the electron stayed in metal-centred orbitals. Thus the transition is called metal-centred (MC). The new configuration is called ^{3}MC since the two unpaired electrons are parallel and form a triplet. If one more electron is promoted from a t_{2g}-orbital to an e_g-orbital, and they are all parallel, the configuration would look as in Figure 6.4 (^{5}MC). This is also a metal-centred state, but since the four unpaired electrons form a quintet it is called ^{5}MC.[13][15] The ^{5}MC-state is lower in energy than the ^{3}MC since the energy gained from having four electrons parallel is larger than the energy lost in promoting one more electron to an e_g-orbital.[17]

Instead of drawing the orbital energy-level diagram showing the position of single electrons, one can draw the electronic states of the whole system, reflecting the energy of all electrons in different configurations at once. The states are then named after the different transitions that result in the different states. Such a diagram is called a Jablonski diagram, and is drawn for FeL_6 in Figure 6.5 a.[18] The ground state (GS) configuration was shown in Figure 6.3 b and the other configurations in Figure 6.4.

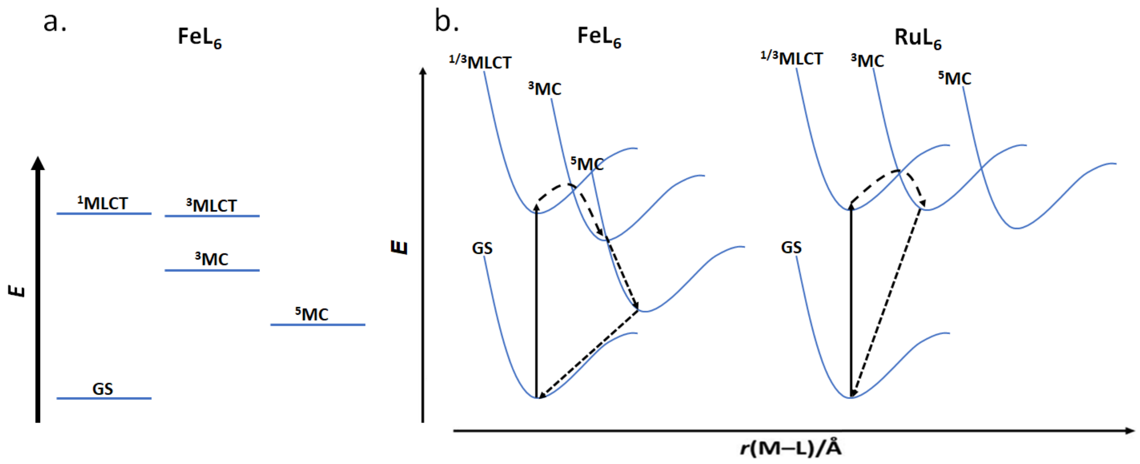

Figure 6.5: a, Jablonski diagram for an FeL_6-complex with relevant electronic states. b, comparison of relevant potential energy curves for a RuL_6-complex and an FeL_6-complex. Also included selected relaxation pathways.[13]

The potential energy curves in Figure 6.5 b gives more information than the Jablonski diagram since they give the electronic state energies as functions of the reaction coordinate r(M-L) measured in Ångström. r(M-L) is the average length of the metal-ligand bonds. As seen in Figure 6.5 b, the different electronic states have different energies at different reaction coordinates, and the lowest energy distance can differ between electronic states.[19]

According to MO-theory, the partly covalent bond between the metal and the ligands implies that their orbitals mix to form a set of new orbitals for the whole system, see Figure 6.3 c. This means that the picture is not as simple as the orbitals for the configurations in Figure 6.4. Due to this, also the transition rules do not apply strictly anymore, however they do still say something about what is a more probable transition i.e. the intensity in an absorption spectrum.[12] What defines the strength of an electronic transition is the overlap between involved orbitals.[17]

It is, however, common that the system can relax to an electronic state by different kinds of transitions where the spin can change and the metal-to-ligand distance can change. For transition metal complexes intersystem crossing (ISC), that is a non-radiative transition between electronic states of different spin, can occur on a rather fast timescale.[20] Selected relaxation pathways and some timescales are shown for the system in Figure 6.5 b. Also indicated in Figure 6.5 b is that to be able to change electronic state the system needs to go through the crossing point of the two electronic states.[13] The energy difference from the current electronic state energy minimum to the crossing point makes up an activation barrier. The crossing point is reached via vibrational levels i.e. the activation barrier is overcome by vibrational energy.[20]

6.3 N-Heterocyclic Iron-Carbenes

A dye suitable as sensitizer in DSSCs should ideally absorb a lot of light over the whole visible spectrum and have high quantum yield for charge separation. Further, it should ideally have a long enough excited state lifetime for the photochemical reaction to occur and be stable in both oxidized and reduced states.[2][10] Several types of molecules can be used to perform these tasks, but the traditional ones are Ru-complexes, i.e. molecules based on ruthenium surrounded by organic ligands.[3] Within the research area there is an urge to replace the expensive and rare ruthenium by other elements.[2][3][21] Iron, being in the same group as ruthenium in the periodic system and thus has similar properties, has been a desirable candidate to replace ruthenium. Iron has several good properties such as being highly abundant (hence it is inexpensive), non-toxic and highly chemically stable.[7]

The challenge with Fe^{II}-complexes compared to Ru^{II}-complexes is that the excited ^{3}MLCT-state and the MC-states are energetically inverted, as can be seen in Figure 6.5 b. This means that for Fe-complexes the electron can relax into the MC-states on a timescale faster than injection into the semiconductor conduction band, whereas for Ru-complexes it can not.[2][13] To try to make Fe-complexes better dyes in DSSCs, attempts to stabilize the ^{3}MLCT-state and destabilize the MC-states are made. This would make the energy difference between the states smaller which prolongs the lifetime of the ^{3}MLCT-state since the driving force to switch would be less. In Fe-complexes, this is achieved by varying the structure of the organic ligands. An example of an Fe-complex, synthesized by the group of Wärnmark at Lund University, can be seen in Figure 6.6.[13] If the two ligands are equal, the complex is called homoleptic, and if they are different the complex is called heteroleptic.[22]

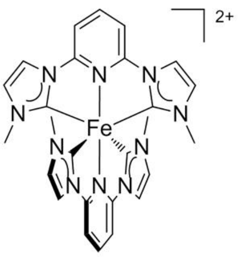

Figure 6.6: An example of a carbene Fe^{II}-complex synthesized by the group of Wärnmark at Lund University.

To stabilize the ^{3}MLCT-state and destabilize the MC-states one can take the following approaches[13]:

1. Extension of the π-system
2. Electron-withdrawing groups on the ligands
3. Strong σ-donation to metal centre from ligands
4. More octahedral structure

Since the binding of the ligands to the metal is mostly comprised of σ-donation to the e_g-orbitals on iron, it is important to work with approach 3.[13] A group of ligands that are able to strongly donate electron density to transition metals through σ-donation is N-heterocyclic carbenes. N-heterocyclic carbenes, or NHCs, are defined as heterocyclic species containing a carbene carbon and at least one nitrogen atom within the ring structure. Further, a carbene is defined as a compound containing a divalent carbon atom with a six-electron valence shell. The carbenes are inductively and mesomerically stabilized by placing N-atoms next to the divalent carbon (carbene carbon).[23] The complex in Figure 6.6 is an example of a homoleptic NHC.[13]

For approach 3, the sp^2-hybridized carbene carbon holds two unpaired electron in an sp^2-orbital that can effectively donate electron density into the e_g-orbitals of iron.[23][13] This results in a stronger ligand-field strength. The splitting of the d-orbitals becomes larger, thus the e_g-orbitals are raised in energy. This results in a destabilization of the MC-states since the MC-transitions will have higher energy.[13] A more octahedral structure, as suggested in approach 4, would also increase the ligand-field strength and destabilize the MC-states in the same way as approach 3. This is because a more octahedral arrangement of the ligands gives a better overlap with the d-orbitals and thus stronger σ-donation.[24]

In approach 1 and 2, the stabilization of the MLCT-states are what comes into play. By extending the π-system in the ligand, the energy of π^* is lowered. By putting electron-withdrawing groups on the ligand, the electrons are dragged out of the π-system which also lowers the energy of π^*. If π^* is lowered in energy, the MLCT-transitions would require less energy and thus the MLCT-states would be stabilized. This would however change the absorption spectrum of the molecule towards longer wavelengths.[24]

To be able to attach the dye to the semiconductor surface an anchoring group is needed that can bind to the semiconductor surface. The anchoring group is supposed to facilitate the injection of electrons from the dye into the semiconductor.[25][2] Anchoring groups are incorporated in the ligands as side groups. The anchoring group should ideally be electron withdrawing to promote the excited electron to go (from metal-centred orbitals) to ligand-centred orbitals near the semiconductor.[2] If the dye complex is heteroleptic and the ligand not comprising the anchoring group instead is electron donating, the electron is upon excitation pushed and pulled towards the semiconductor and this effect is thus called push-pull.[26] In this thesis two different anchoring groups are used; namely the often used carboxylic anchoring group and the non-typical imidazolium anchoring group, see Figure 5.1. The carboxylic anchoring group redshifts the absorption of carbenes which is a good thing, since the absorption then covers more of the solar spectrum.[7] The carboxylic group is also an electron-withdrawing group attached to the ligand, which helps to stabilize the MLCT-states through approach 2, and thus prolongs the lifetime.[13]

6.4 Optical Properties

Atoms can interact with photons in three fundamental, resonant ways; via absorption, spontaneous emission and stimulated emission. In molecules and materials, that have more complicated energy levels and transition rules than atoms, it is still the same three fundamental interactions.[16][14] Thus by investigating optical properties such as absorption and emission spectra, one can learn about the transitions and the energy states of the, in the scope of this thesis, molecule.[14]

If an impinging photon has about the same energy as a transition between two states in a system (or the same frequency ν_0), it has a probability to be absorbed. This probability is quantized as the transition cross section (σ). σ is a frequency-dependent measure and expressed in area [cm^2]. In Figure 6.7 the transition cross section σ is plotted as a function of photon frequency ν.[16] If absorbed, an electron is promoted from one energy level to a higher one, so the system enters a higher energy state. In molecules, an energy state is often broadened by several vibrational states existing in the same electronic state. Therefore photons with different energies within a sufficiently small energy span can still excite the same electronic state.[14] This can be seen in Figure 6.7 since the cross section is a function of finite width. This width is often referred to as the linewidth ($\Delta\nu$). It is used to characterize the spectral shape of a transition and is defined as the full width at half maximum (FWHM).[16]

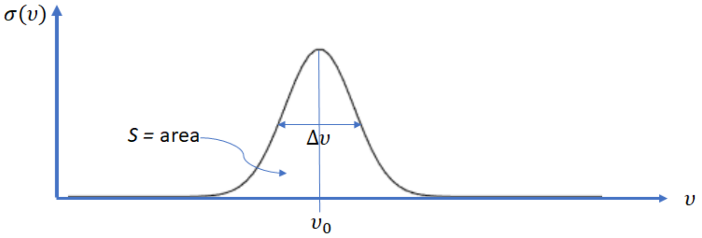

Figure 6.7: A typical transition cross section σ as a function of frequency ν with indicated central frequency ν_0, linewidth at FWHM $\Delta\nu$ and oscillator strength S.

If the transition cross section is integrated over the whole frequency-space, the result is the area under the curve in Figure 6.7, S.

$$S = \int_0^\infty \sigma(\nu)d\nu \tag{1}$$

The oscillator strength, or S, thus is a measure of how strong the interaction is between the molecule and the photon for a given transition.[16]

In all the experiments within this thesis, molecules are dissolved in a relatively non-interacting solvent (acetonitrile). It can therefore be assumed that the concentration throughout the sample is the same.

If light of intensity I_0 is impinging on the sample, and light of intensity I_t is transmitted through the sample, the absorbance, A, or optical density, OD, is defined as

$$A = OD = \log\left(\frac{I_0}{I_t}\right) \tag{2}$$

The absorbance of the sample can be related to the thickness of the sample, l, the concentration of the sample, c, and a material specific constant, ϵ, through the Beer-Lambert law

$$A = lc\epsilon \tag{3}$$

The constant ϵ is wavelength dependent and a property of the chemical substance stating how much light it absorbs, often given in the unit $[\frac{1}{\text{mol}\cdot\text{cm}}]$.[14] ϵ is called the extinction coefficient or the molar attenuation coefficient.[22]

Emission is when a system relaxes from a higher electronic state to a lower, i.e. an electron moves to a lower energy level, by sending out a photon. This process can be either stimulated or spontaneous. For stimulated emission, a photon matching the transition energy is needed, and instead of being absorbed a photon of equal polarization, phase and direction is sent out. Spontaneous emission is not triggered by any external photon. Both processes though requires that an electron in the system can relax to a lower lying energy level.[14][16]

In a molecule each electronic state has a fine structure of vibrational states within it, see Figure 6.8. The vibrational states lead to a broadening of the observed transitions and depending on the resolution of the spectrometer and the temperature, one can resolve the single vibrational states on their own. An electronic transition is thus always from a given vibrational state to another vibrational state in the other electronic state (and can therefore be called a vibronic transition). The probability of a vibronic transition is governed by the vibrational wavefunction overlap at a given reaction coordinate. This is called the Franck-Condon principle. In Figure 6.8 examples of vibronic transitions with big wavefunction overlap are indicated by arrows.[14]

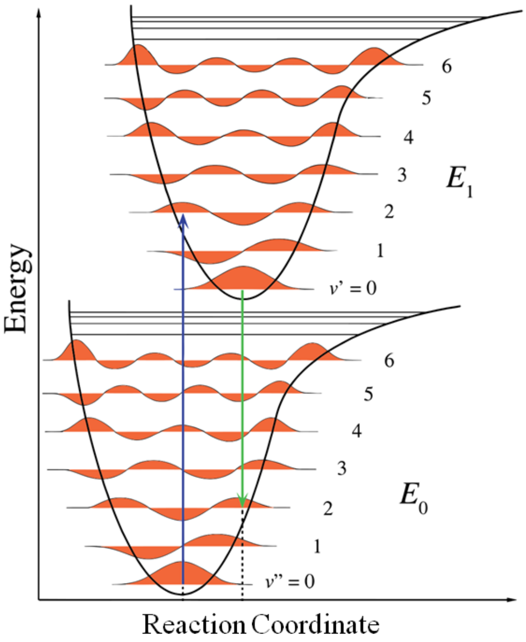

Figure 6.8: The electronic ground state E_0 and first excited electronic state E_1 potential energy curves with indicated vibrational levels. For some vibrational levels the vibrational wavefunctions are drawn and two probable vibronic transitions are indicated by the arrows. Image taken from https://commons.wikimedia.org/wiki/File:Franck_Condon_Diagram.svg.

For organic dye molecules, the common case is the one illustrated in Figure 6.8. The molecule usually absorbs light from the lowest vibrational level in the electronic ground state, as indicated by the blue arrow. The excited electron then non-radiatively de-excites to the lowest vibrational level within the upper electronic state before it can de-excite to the electronic ground state by spontaneous emission. This introduces an energy shift between the excitation energy and the emission energy, called Stokes' shift. The excitation energy is always higher than the emission energy.[14] If the molecule is excited to an electronic state higher than the first excited state, Kasha's rule states that the emission of appreciable yield will occur only from the lowest excited electronic state of a given multiplicity. There are however several cases where Kasha's rule does not longer apply and it should be considered as a guideline.[18]

Fe^{II}-carbene-complexes are rarely emissive at room temperature due to the short lifetime. The system simply does not stay long enough in the excited electronic ^{3}MLCT-state to be able to spontaneously emit a photon. However, emission at room temperature has been seen for the first time for an Fe^{III}-carbene-complex with a lifetime of around 100 ps. The reason for this difference is mainly that the transition from the ^{3}MLCT-state to the ground state for Fe^{II}-carbene-complexes is classically forbidden because of selection rules, while the emissive transition in the Fe^{III}-carbene-complex is not.[9][27]

Materials and molecules can also interact with photons in non-resonant ways. Scattering processes belong to this category, and can involve transitions that occur via virtual states. Two kinds of scattering processes are shown in Figure 6.9; Rayleigh scattering and Raman (Stokes) scattering.

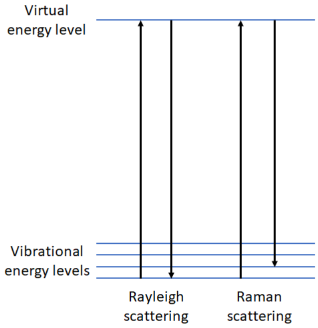

Figure 6.9: Schematic principal of two types of scattering processes; Rayleigh scattering and Stokes Raman scattering.

Rayleigh scattering is also called elastic scattering since the incoming photon keeps its energy, it just changes direction. The Rayleigh scattering intensity is wavelength dependent and proportional to $1/\lambda_0^4$ where λ_0 is the wavelength of the photon. Stokes Raman scattering is an inelastic process where the photon loses energy to the system in the form of vibration (or rotation) and can change direction. The energy shift of the photon thus corresponds to the energy distance between the vibrational states involved, as seen in Figure 6.9.[16]

6.5 Steady-State Spectroscopy

Steady-state spectroscopy includes in this thesis absorption, emission and excitation spectroscopy. In contrast to the time-resolved technique explained in the following section, steady-state techniques do not exhibit temporal resolution i.e. they only give an accumulated signal. In absorption spectroscopy, the ground state of the molecules are investigated, whereas in emission spectroscopy the excited states are monitored. Excitation spectroscopy is used to probe which state is the origin of potential emission, this is done by comparing the excitation spectrum to an absorption spectrum.[14]

The basic principle of absorption spectroscopy is to shine light of a certain wavelength and of known intensity on a sample and then measure what light intensity is transmitted. From the original intensity and the transmitted intensity, the absorbance can be calculated by using equation 2 (this is usually done directly by the instrument). Since other parts of the sample than the molecule of interest can absorb, spectrometers can be designed to have two sample holders, one for the full sample and one for the reference.[14] For absorption spectroscopy, mainly the UV/VIS spectrometer ”Perkin Elmer Lambda 1050” was used in this thesis. A schematic of the instrument is seen in Figure 6.10.[28]

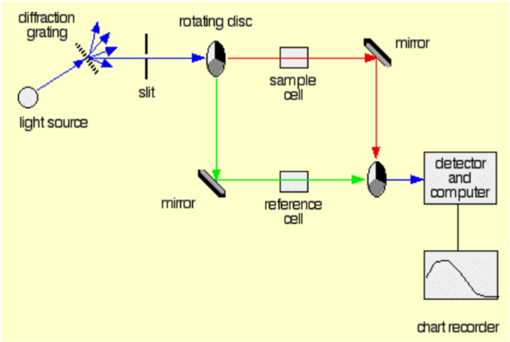

Figure 6.10: Schematic principal of the spectrometer used for absorption spectroscopy, ”Perkin Elmer Lambda 1050”. Image taken from [29].

The absorption spectrometer has two light sources; a Deuterium and a Tungsten halogen lamp.[28] The selected wavelength range is scanned by tilting the diffraction grating, seen in Figure 6.10. The desired wavelength is selected by a slit and passing to a rotating disc that sends the light either through the full sample, the reference sample or blocks the beam for a background correction. After the sample or reference the beams pass another rotating disc analogous to the first one to combine the beams onto a photomultiplier tube (PMT) for detection.[29]

The basic principle of emission spectroscopy is to excite the sample using light of a particular wavelength, and then probe the light coming out of the sample in a selected wavelength range. In excitation spectroscopy, the excitation wavelength is scanned over a selected wavelength range and the light emitted by the sample is probed at a specific wavelength. For emission and excitation spectroscopy the spectrometer ”Horiba Fluorolog 3 - Spectrofluorometer” was used. A schematic of the instrument is seen in Figure 6.11.[30]

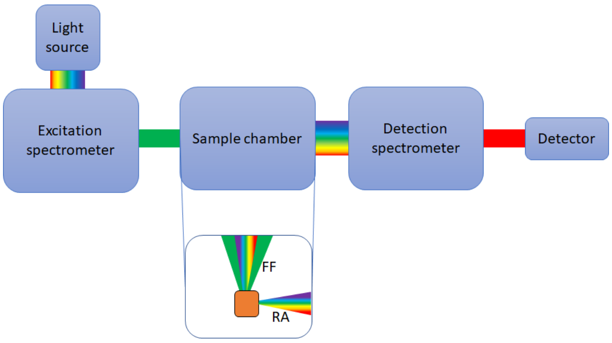

Figure 6.11: Schematic principal of the spectrometer used for emission and excitation spectroscopy, ”Horiba Fluorolog 3 - Spectrofluorometer”. In the figure, the difference between front face (FF) and right angle (RA) collection has been indicated.

As seen in Figure 6.11, light is guided from a light source (in this machine a Tungsten arc lamp) to the excitation grating (in the excitation spectrometer in the figure). For emission spectroscopy a fixed wavelength is selected by this grating, for excitation spectroscopy the wavelength is scanned by tilting the grating. The selected wavelength reaches the sample placed in the sample compartment module. The emission can be collected from two different geometries, either front face (FF) or at right angle (RA), and is relayed to the emission spectrometer. For emission spectroscopy, the grating in the emission spectrometer scans over the selected probing range and each wavelength is detected individually. For excitation spectroscopy, the grating in the emission spectrometer is set to the selected wavelength and the light intensity is detected. The PMT detector converts the photons into a current that is read out by the software and a spectrum is obtained.[30]

6.6 Transient Absorption Spectroscopy

Transient absorbtion spectroscopy, TAS, is in this thesis used to study the kinetics of electrons and their pathways, especially the injection of electrons into TiO_2 for half-cells.[7] Most photophysical and photochemical reactions happen on the timescale $10^{-14} - 10^{-9}$ s, thus it is needed to probe the system on this timescale to be able to understand it.[31] This is not the steady-state case of the system, but the transients before the system reaches ground state.[22] The setup, Figure 6.12, can be used to investigate processes on a timescale of 100 fs - 10 ns, limited by artefacts for ultrafast times and the length of the long delay line for long times. Therefore, transitions ^{1}MLCT → ^{3}MLCT will not be seen with this setup since they are too fast and processes on longer timescale than ns will not be investigated.[8]

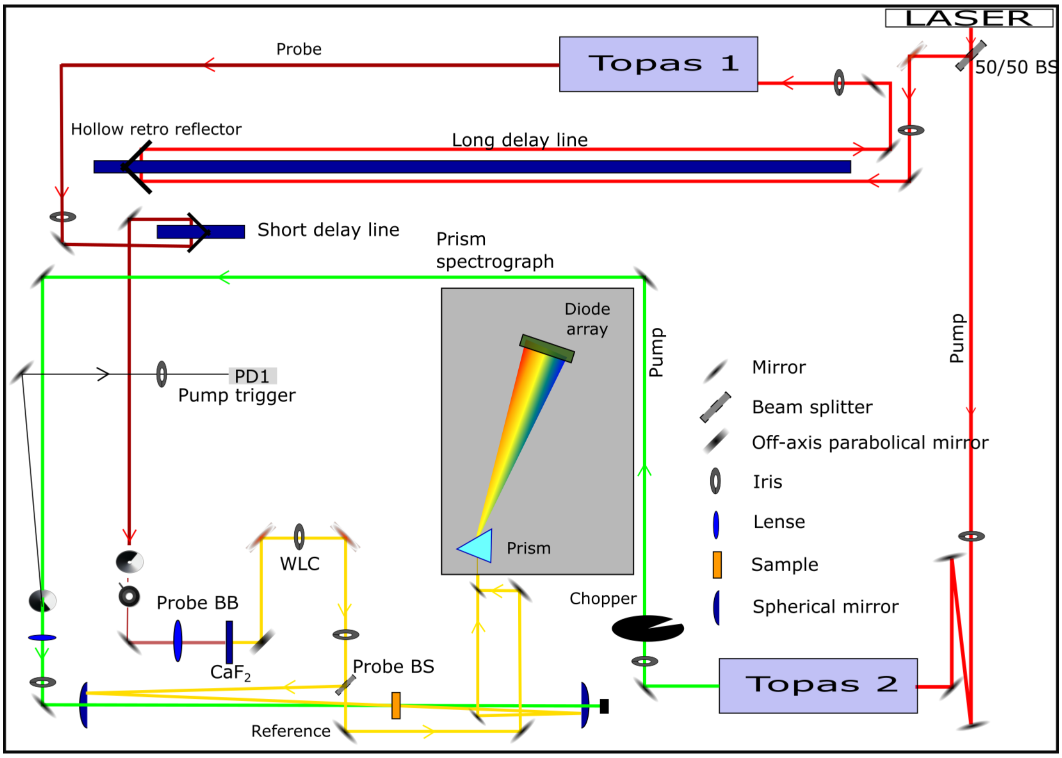

Figure 6.12: Schematic of the transient absorption spectroscopy laser setup, built by Pavel Chábera at Chemical Physics Lund University.

The light used for TAS is generated by a Ti sapphire laser indicated in the top right corner of Figure 6.12. The laser is producing 800 nm, 50 fs long light pulses at repetition rate 1 kHz and power 6 W. The laser beam is split into two equal parts; one that will become the pump beam and one that will become probe and reference beams. The pump beam is altered to the desired excitation wavelength by the optical parametric amplifier (OPA) named "Topas 2" in Figure 6.12. The light is guided towards the sample but passes a chopper on the way to block out every other pulse, and a filter wheel to fine tune the intensity. After passing the sample the pump beam is sent to a beam dump.[9]

The other half of the fundamental laser beam is sent through a long delay line that can alter its path length during the experiment and thus add different delay times to the pulse compared to the pump pulse (also a short delay line is in the setup, but it was kept at a fixed distance in this thesis). The wavelength of the pulses is changed to 1300 nm by sending the beam through an OPA named "Topas 1" in Figure 6.12. The beam continues through a filter wheel used to fine tune the intensity before the beam reaches the CaF_2 crystal. Due to a non-linear interaction between the crystal and the beam, the pulses are broadened in frequency to white-light continuum (WLC). The WLC beam continues to a beam-splitter that divides the beam into a probe beam and a reference beam. The probe beam is focused to the sample overlapping with the pump beam, and is then collimated to an entrance pinhole of the prism spectrograph. The reference beam is instead guided around the sample and to another entrance pinhole just below the first one, of the prism spectrograph. Inside the spectrograph the beams are travelling the same path (but separated in two different horizontal planes), first to prisms that disperses the white light and then to diode arrays that detect the two beams and send the signals to a computer.[9]

What is measured in transient absorption spectroscopy is how the difference absorbance of the sample changes at different times after the sample has been excited (pumped). The difference absorbance (ΔA) means the absorbance when the sample is excited minus the absorbance when the sample is not excited. This is why every other pump beam is blocked by the chopper, to get the absorbance of the unpumped sample to be able to calculate the difference. This is also why it is important to get a good overlap between the probe beam and the pump beam on the sample. The pump beam wavelength is usually selected to excite the sample in one of its absorption peaks. The polarization between the pump and probe beams is set by a polarizer to the "magic angle" 54.7° to eliminate polarization and photoselection effects.[31]

The data obtained from TAS is a three-dimensional matrix, since the difference absorption ΔA is measured as a function of both wavelength and time. For the sake of clarity, data is usually presented in two dimensions at the time; at a fixed time giving $\Delta A(\lambda)$ called the TA spectrum or at a fixed wavelength giving $\Delta A(t)$ called the TA kinetic. Several different decay models can be used to fit the data. From the fitting, the lifetimes of the different decay components in the TAS data are obtained.[31] The data is corrected for chirp, the phenomenon that ultrashort pulses contain a broad range of frequency components that travel at different speeds making the pulses stretched over time.[16] In this thesis, the data obtained are fitted by using global analysis with the time-dependence entering the model as a sum of sequential exponential functions representing the different components decaying with their own lifetimes τ, see Equation 4.[32][33]

$$A_1 e^{\frac{-t}{\tau_1}} + A_2 e^{\frac{-t}{\tau_2}} + A_3 e^{\frac{-t}{\tau_3}} + A_4 e^{\frac{-t}{\tau_4}} + ... \tag{4}$$

In TAS, mainly three different effects can affect the TA spectrum obtained. If molecules in the sample are excited by the pump beam, there will be less molecules excited by the probe beam when the sample is unpumped than pumped. This results in a negative difference absorbance signal called ground state bleach (GSB), usually having the shape of the inverted absorption spectrum of the molecule. For the sample excited by the pump beam, the incoming photons of the probe beam can cause stimulated emission. The stimulated emission photons are also detected which gives less absorbance for the pumped sample than the unpumped sample, resulting in a negative difference absorbance signal called stimulated emission (SE). The molecules excited by the pump beam are able to absorb a part of the probe beam to be excited to yet another state that is not accessible from the ground state. This means that more light would be absorbed for the pumped sample than the unpumped sampe, giving a positive difference absorbance signal called excited state absorption (ESA). Another possible signal would be a GSB signal for a product formed from the sample when reacting with light, for a half-cell possibly the oxidized dye.[31]

6.7 Solar Cell Characterization

A solar cell is a device which absorbs light from the sun and turns it into electricity. How good a solar cell is at doing this can be determined by measuring characterization parameters such as different efficiencies, the open circuit voltage (V_{oc}), the short circuit current density (J_{sc}) and the fill factor (FF). The different parameters are probed at given light intensities, most commonly given in air mass (AM). The air mass is the optical path of the light through the atmosphere of Earth normalized to the thickness of the atmosphere, at a given location. How much light intensity the sun delivers depends on a lot more factors than just the location, but a commonly used intensity for solar simulators is 1 kW/m^2 which is defined as AM1.5.[34]

Upon illumination, the solar cell produces a voltage (V) and a current density (J). The voltage and current density depend on each other through the resistance connected to the solar cell and the possible working points of the solar cell are usually plotted as a graph of current density versus voltage. This is called the IV-characteristic and typically looks like in Figure 6.13 (blue curve). Two working points easy to probe are the open circuit voltage (infinitely high resistance, thus the voltage at which the current density is zero) and the short circuit current (zero resistance, thus the current density where the voltage is zero). Therefore, the parameters have become important characteristics for solar cells. The parameters are indicated in Figure 6.13.[34]

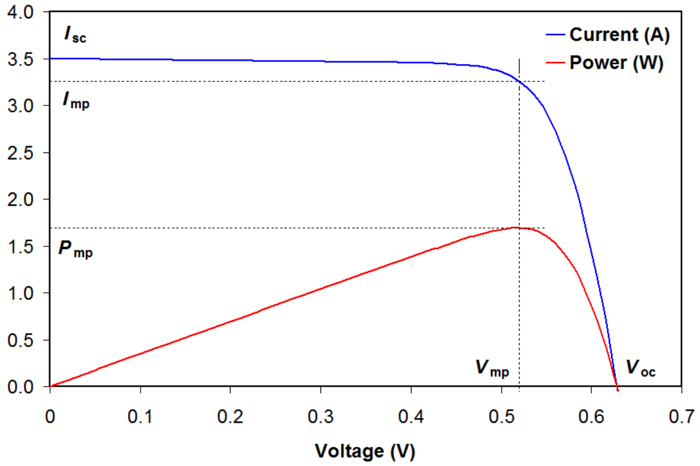

Figure 6.13: A typical IV-characteristic for a solar cell (blue) and also the corresponding power as a function of voltage (red). In the graph the current I instead of the current density$J$ is plotted, this however does not effect the shape of the curve. Important characterization parameters are indicated in the graph. Image taken from https://commons.wikimedia.org/wiki/File:I-V_Curve_MPP.png.

If the current density J is multiplied with the voltage V the power density P (in [W/cm^2]) is obtained.[34]

$$P = J \cdot U \tag{5}$$

The power density is plotted versus the voltage in Figure 6.13 (red curve). From such a graph, the point of maximum power P_{mp} is easily identified. In this point the maximum power voltage V_{mp} and maximum power current density J_{mp} can be obtained. Often, the two rectangles spanned by V_{oc}, J_{sc} and V_{mp}, J_{mp} are compared in the characterization parameter fill factor, FF. The fill factor is defined as how much the second rectangle fills the first one.[34]

$$FF = \frac{V_{mp} \cdot J_{mp}}{V_{oc} \cdot J_{sc}} \tag{6}$$

Generally, the higher V_{oc}, J_{sc} and FF the better.[34]

By efficiency, a lot of different definitions can be meant. In this thesis, the conversion efficiency, η, will be used. The conversion efficiency is defined as the ratio of the power density extracted at the mp point to the intensity of the light it is illuminated with.[34]

$$\eta = FF \cdot \frac{V_{os} \cdot J_{sc}}{I_{sun}} \tag{7}$$

The efficiency is the ultimate characterization parameter when it comes to cost effectivity.[34] The best DSSC today has an efficiency of 11.9 %. For comparison, the best silicon solar cell has an efficiency of 27.6 % at AM1.5.[35]

Incident photon-to-current conversion efficiency, or IPCE, is defined as the ratio between the collected carriers and the incoming photons which is the same as the external quantum efficiency of a solar cell.[4] To measure the IPCE, the setup in Figure 6.14 was used. The light from a Xe-lamp is sent to a monochromator that scans the wavelength of the light sent to the sample. At each wavelength, the generated photocurrent in the solar cell is measured by the multimeter. The photocurrent as a function of wavelength can be recalculated to the IPCE as a function of wavelength by using a reference cell with known

IPCE-spectrum.[36]

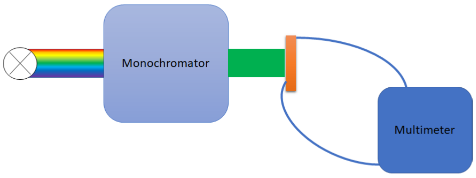

Figure 6.14: Schematic of the IPCE measurement setup at Physical Chemistry, Uppsala University.

Photon induced absorption, or PIA, is a technique that can be used to investigate dye-sensitized solar cells under illumination conditions comparable to sunlight. By measuring the transmission of white light when the sample is excited by a laser compared to when it is not excited by a laser, the difference in absorbance can be calculated. When the sample is a transparent solar cell (fabricated for measurements only), one can see if the excited dye is regenerated by the electrolyte or not. If one wants to see the oxidized dye difference absorbance spectrum, the solar cell can be filled with inert electrolyte. The setup for PIA used in this thesis can be seen in Figure 6.15.[37]

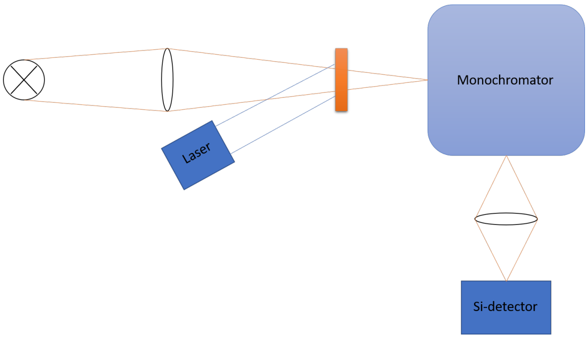

Figure 6.15: Schematic of the photon induced absorption setup at Physical Chemistry, Uppsala University.

White light to simulate the sun is generated by a tungsten-halogen lamp. The light is sent through the transparent sample and focused to the monochromator. The monochromator selects one wavelength of the transmitted light at the time to be sent to the Si-detector. The transmitted light is detected and averaged at the same time (minimum 20 times and maximum 200 times, depending on when the averaging reaches a sufficiently low standard deviation). Both pumped and unpumped sample transmission is detected at each wavelength to be able to construct the change in transmission that is recalculated by the software to the difference in absorbance.[37]

6.8 Density Functional Theory

Density functional theory (DFT) is a technique within quantum mechanics widely used to calculate the electron density of different molecular states. From this electron density, many other interesting properties such as Kohn-Sham molecular orbitals, the energy of a state, and the spin density of a state can be calculated.[38]

In the foundations of quantum mechanics, it is known that the energy of a system is governed by the Schrödinger equation

$$H\Psi = E\Psi \tag{8}$$

where H is the Hamiltonian operator, a quantum mechanical operator giving the energy E of a state when operating on the wavefunction Ψ of that particular state. It is actually so that if the wavefunction Ψ of a state is known, everything about that state is known since different quantities can be calculated by using quantum mechanical operators. Finding the wavefunction of a state, especially for a complex molecule, can however be quite difficult.[38]

It is however possible, for the ground state of a system, to guess the wavefunction. According to the variational principle, the energy E' of the guessed wavefunction Ψ' is always larger than the energy of the true wavefunction. Only if the guessed wavefunction in fact is the ground state wavefunction their energies are the same.

$$E' \quad \rangle \quad E \tag{9}$$

In quantum mechanics there are different approaches how to guess ground state wavefunctions, and the variational principles can be implemented by computer programs to minimize the energy until the energy step taken in each cycle is sufficiently small. The system has then converged and obtained is a sufficiently good guess of the wavefunction and energy. This is called the self-consistent field approach.[38]

In density functional theory the problem of guessing the complicated many-particle ground state wavefunction is avoided. Instead one works with the electron density, which is much easier to guess if one knows how the geometry of the molecule looks like. The electron density of course does not contain as much information as the true wavefunction, but it can be shown that the most important quantities can be calculated from the electron density. It can also be shown that the variational principle applies to electron densities as well. Therefore, the same computing strategy can be used to minimize the energy for a guessed electron density. The variational principle for the electron density $\rho(\vec{r})$ uses not a wavefunction-based quantum mechanical operator, but a functional F.

$$E_0 = \min_{\rho \to N} \left(F[\rho(\vec{r})] + \int \rho(\vec{r}) V_{Ne} d\vec{r} \right) \tag{10}$$

A functional is a mathematical concept that takes a function as parameter and delivers a number as result. Here, the functional F takes in the electron density $\rho(\vec{r})$ and delivers an energy that together with the external potential V_{Ne} energy contribution gives the energy of the specific electron density. When the electron density energy is minimized as $\rho \to N$ (N is the number of particles and here means the true electron density of the many particle state), the ground state energy E_0 will be obtained.[38]

The functional F can be split into different parts of different physical meaning. Since the explicit expression of the functional F is not known, it was a struggle to split it in such a way, so that the bigger part of the energy could be calculated exactly and as little part as possible needed to be approximated. The strategy of splitting the kinetic energy into the kinetic energy in a non-interacting reference system and the rest, introduced by Kohn and Sham became the widely used one.

$$F[\rho(\vec{r})] = T_s[\rho(\vec{r})] + J[\rho(\vec{r})] + E_{xc}[\rho(\vec{r})] \tag{11}$$

Here the functional F is split into the non-interacting kinetic energy part, T_s, a Coulomb repulsion energy part, J, and an exchange-correlation energy, E_{xc}, where everything else is accounted. This means that the exchange-correlation energy consists of energy contributions coming from the residual parts of the true kinetic energy, T_c, and the non-classical energy effects, E_{ncl}, consisting of self-interaction correction, exchange and electron correlation effects.[38]

$$E_{xc}[\rho(\vec{r})] = T_c[\rho(\vec{r})] + E_{ncl}[\rho(\vec{r})] \tag{12}$$

In density functional theory, the accuracy of the calculations depend on how good the approximation of E_{xc} is. Many different functionals are available as approximations, and in this thesis B3LYP* will be used. B3LYP* is a hybrid functional meaning that it contains parts coming from approximate density functionals for exchange and parts coming from exact Hartree-Fock exchange.[38] This functional is suitable for DFT calculations of first row transition metal complexes.[39]

To be able to calculate excited states, one needs to know how the system responds to a time-dependent pertubation. That is the light coming in with the time-dependent electric field of frequency $\omega(t)$. The system responds to the pertubation in its dipole moment by a response in the mean polarizability $\alpha(\omega)$:

$$\alpha(\omega) = \sum_I \frac{f_I}{\omega_I^2 - \omega^2} \tag{13}$$

When $\omega = \omega_I$, that is when the light has the same frequency as one of the allowed excitation frequencies of the system ω_I, equation 13 diverges. This means that the mean polarizability $\alpha(\omega)$ has poles at the excitation frequencies ω_I with residues f_I becoming the oscillator strengths. In this way frequencies and oscillator strengths can be calculated for excitations from the ground state of a system. The technique is called time-dependent density functional theory, or TD-DFT.[38]

7 Experimental Procedures

7.1 Extinction Coefficient

To be able to calculate the extinction coefficient of a sample several absorption spectra were measured for solutions of known concentration of the sample. All concentrations needed to be below 1 mmol/l in order to avoid agglomeration of the sample, that would affect the absorption. Firstly, a stock solution of known concentration was prepared. The sample was carefully weighted and dissolved in acetonitrile in a volumetric flask. The absorption spectrum of the stock solution was measured and if it was too highly absorbing the stock solution was diluted by an appropriate factor. Carefully measured amounts of the stock solution were then transferred to 5 volumetric flasks and diluted with distilled acetonitrile. The dilution coefficients used for the dilution series are stated in Table 7.1.

Table 7.1: Table containing the dilution coefficients of the different solutions prepared for the extinction coefficient measurements.

Solution	**Dilution coefficient**
5	10
4	25/2
3	50/3
2	25
1	50

Absorption spectra were then measured for all solutions using the same settings as for the stock solution. A 1 cm quartz cuvette was used for all measurements, and was rinsed with acetonitrile and blown dry with nitrogen between the measurements. At each wavelength measured, a line was fitted to the absorbance as a function of the solution concentration. From the slope of each line, the extinction coefficient at that specific wavelength was calculated by using Equation 3. The extinction coefficients were plotted as a function of wavelength.

The extinction coefficient was measured for the samples stated in Table 7.2.

Table 7.2: Samples for which the extinction coefficient was measured with the stock solution concentrations.

Sample	**Stock sol. c (μmol/l)**
FeCAB26	156.7
FeCAB26 ligand	95.1
FeCABCN2	47.9

7.2 Stability Measurement

The long-term stability of FeCABCN2 was investigated by preparing a sample in a cuvette and measuring the absorption several days in a row. Firstly, FeCABCN2 was dissolved in MeCN and put in a 1 mm cuvette. The absorption was measured and checked so the concentration was sufficiently low (absorbance below 0.2). The cuvette was sealed with parafilm and not opened during the measurement days. The cuvette was stored in a drawer to avoid degradation induced by light. The same absorption spectrum (from 250 nm to 850 nm) was measured almost every day for two weeks by Nils Rosemann at Chemical Physics, Lund University. The spectra were then plotted together to see potential changes.

7.3 Steady-State Emission

In order to cover the emission over the spectral range of about 200-900 nm a series of measurements were decided on. The series was constructed so that each measurement had a different excitation wavelength that would probe a part of the spectral range partly overlapping with the range covered by the next excitation wavelength. Firstly, the whole measurement series was carried out on just a 1 cm quartz cuvette filled with acetonitrile. This made up the references for the measurement series. Secondly, a small amount of sample was dissolved in the acetonitrile used for the reference measurements and again put in the cuvette. An absorption spectrum was measured to assess whether the concentration of sample was too high, the rule of thumb being to have an optical density below 0.1. If the concentration was too high, the solution was diluted with acetonitrile. Finally, the same emission measurement series was performed with the dissolved sample, using the same settings as for the references.

For peaks in the emission spectra, sometimes an excitation spectrum was measured. The excitation spectrum was then used to give information about if the peak was true emission or not. Also data analysis was performed to try to sort Raman peaks out from true emission peaks. The emission spectra were plotted together after carefully removing the reference measurements and artefacts.

Steady-state emission characterization was carried out for the samples stated in Table 7.3.

Table 7.3: The samples for which the steady state emission was investigated, what excitation wavelengths were used for emission spectra and what emission wavelengths were used for excitation spectra.

Sample	**Excitation λ (nm) for emission spectra**	**Emission λ (nm) for excitation spectra**
FeCAB26	502, 450, 400, 350, 325, 300, 260, 244	425
FeCAB26 ligand	502, 450, 400, 350, 325, 300, 260, 244	425, 320
FeCABCN2	243, 296, 350, 390, 425, 470, 528	500, 350

7.4 Half-Cell Fabrication

For transient absorption measurements performed on FeCAB26 and FeCABCN2, half-cells were prepared to be able to measure the injection of electrons into TiO_2. Half-cells with Al_2O_3 films were prepared to serve as references, since electrons can not be injected into the Al_2O_3 (the Al_2O_3 conduction band is too high in energy). Half-cells are not functional solar cells, since they do not contain any electrodes or electrolyte, therefore non-conducting glass was used for their preparation. The half-cells were prepared in three different steps.

Firstly, films of TiO_2 and Al_2O_3 were prepared on microscopy glass slides. The glass slides were carefully wiped with acetone, ethanol and then acetone again before taping them along the sides to a paper, leaving a rectangular area in the middle. TiO_2 and Al_2O_3 pastes were applied in the untaped area by using the doctor blade technique. In the doctor blade technique, a drop of paste is put on one side of the untaped area and is then smeared out by pressing and pulling a glass rod along the area. It was important to keep a low, constant speed and to apply light pressure in order to get a homogeneous film. The films were left to dry for some time in air. The tape was then removed and the films were sintered in an oven at 130°C for about 10 minutes and then 430°C for about 30 minutes. The films were left in the turned off oven over-night to cool down slowly to avoid cracks.

Secondly, the films were sensitized by immersing them in a solution of the either FeCAB26 or FeCABCN2. The solutions were prepared by dissolving an appropriate amount of the molecules in acetonitrile (MeCN). The films were sensitized at least over night, but up to several days. A film was not removed from the sensitization bath until it was time for encapsulation. When taken out of the bath, the films were flushed with acetonitrile and blown dry with nitrogen.

Thirdly, the sensitized films were encapsulated and hence turned into half-cells. A piece of parafilm was cut out to fit the glass slides. A rectangular hole was cut in the parafilm, and the parafilm was placed on the glass slide so that a good sensitized area was selected by the rectangle. A glass piece from a new microscopy slide was cut out to fit the sensitized one. The new glass piece was cleaned with acetone, ethanol and acetone again. The new glass slide was placed to the edge of the rectangle while the area was filled with filtered MeCN, and then slided up to cover the sensitized glass completely. The filling process was repeated until no bubbles of air remained in the cell. The encapsulated film, i.e. the half-cell, was clamped to hold the glass slides together, see Figure 7.1. Absorption spectra were measured for all the fabricated half-cells before they were taken to the TA setup to deem if the films had been sensitized correctly and what excitation wavelength to use for the laser.

Figure 7.1: A finished half-cell fabricated in the labs at Chemical Physics, Lund University.

7.5 Transient Absorption

From the measured absorption spectrum of the half-cell, an excitation wavelength within the maximum absorption peak was selected. The pump beam of the laser was set to this wavelength by altering the OPA settings (OPA named ”Topas 2” in Figure 6.12). The power of the pump beam was set to a reasonable value to get a good signal-to-noise ratio but not so high as to damage the sample. The sample was mounted in the holder and the pump beam was focused a bit behind the sample to get a larger beam diameter than the focused beam to excite the sample, see Figure 7.2.

Figure 7.2: A half-cell sample mounted in the TA laser setup. A cuvette of thickness 1 mm with a sample in solution can be mounted in the same way.

The other part of the beam was aligned on the long delay line and filtered to an appropriate power before it was split into the probe and the reference beams, see Figure 6.12. The probe beam was then focused on the sample within the area excited by the pump beam. The magic angle was set between the beams using a polarizer. Both probe and reference beams were aligned on their paths to the prism spectrograph and inside the prism spectrograph, see Figure 6.12. The energy scale of the measurement was calibrated by using filters with well-known transmission spectra. The measurement was run as long as accumulation of good data was possible. TA measurements were performed for the samples stated in Table 7.4.

Table 7.4: All samples measured with the TA setup and important laser parameters for the individual runs. Note that the sample FeCAB26 in MeCN was measured prior to this thesis by Pavel Chábera at Chemical Physics, Lund University.

Sample	**Excitation** λ (nm)	**Power** (μ**W**)	**Observation range (nm)**	**# of scans**
FeCAB26 in MeCN	500	1000	312.7-1734.9	$\sim$ 20
FeCAB26 on TiO_2	500	580	394.3-1244.0	79
FeCAB26 on Al_2O_3	500	1600	394.3-1244.0	44
FeCABCN2 in MeCN	480	1000	384.0-138.4	21
FeCABCN2 on TiO_2	480	500	388.5-1201.0	55
FeCABCN2 on Al_2O_3	480	500	388.5-1201.0	25

The data from the measurements stated in Table 7.4 were fitted by a sequential exponential model. From the fitting, important lifetimes of decay components were obtained.

7.6 Full-Cell Fabrication

Full-cells, or real solar cells, are needed to perform electrical measurements and assess the solar cell performance. All solar cells were fabricated in Uppsala, as a collaboration with the Boschloo group and Freitag group, at the department of Physical Chemistry. The process is similar to that of the half-cell fabrication. Firstly films of TiO_2 on the conductive glass FTO were prepared by screen-printing. Different layers of TiO_2 were prepared according to Figure 7.3. The screen printing was performed by Hannes Michaels, part of the Boschloo group at Uppsala University.

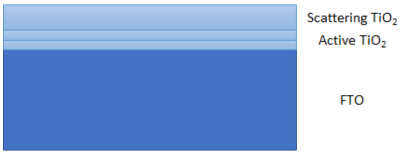

Figure 7.3: The TiO_2 layer structure prepared for the solar cells: two active layers of 30 nm TiO_2 particles followed by a scattering layer of 400 nm TiO_2 particles. The layers are not drawn to scale.

Baths of sensitization liquid of concentration 0.1 mmol/l in MeCN was prepared for FeCAB26 and FeCABCN2. The prepared films of TiO_2 on FTO was cut into appropriate pieces and blown with air to remove glass splinters. The pieces were put in the baths and left over night. In parallel, counter electrodes of two different types were prepared. Pt-electrodes were prepared by smearing a solution of 5 mmol/l H_2PtCl_4 in EtOH on small FTO pieces with a hole drilled in the center. The FTO pieces were put to dry on a hotplate at 76°C to dry and were then baked at 400 °C for 300 min.

To prepare the other kind of counter electrode, consisting of the conductive polymer PEDOT on FTO, electrochemistry was used. A piece of FTO with predrilled holes were mounted in a conducting holder and put in a solution of PEDOT in water. Another piece of FTO of similar size was mounted 1 cm opposite to the first piece, conductive sides facing one another, also in a conductive holder. The FTO pieces were connected to a power aggregate which applied a voltage so that PEDOT was deposited. The drilled FTO piece was rinsed with water, then ethanol and then dried with air. Pieces of the same size as for the Pt-electrode was cut out, making the hole centered.

To assemble the solar cells, the sensitized FTO pieces were merged with counter electrodes according to the scheme in Figure 7.4. The sensitized FTO pieces were taken out of the sensitization baths, rinsed in MeCN and dried in air. A rectangular frame of surlyn was placed according to the scheme in Figure 7.4. A counter electrode was placed on top according to the scheme in Figure 7.4, conductive side facing down, and the cell was sealed using a machine pressing it together while heating. This was done until the surlyn frame had melted sufficiently to avoid leak channels.

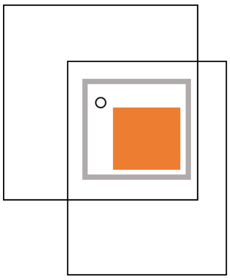

Figure 7.4: A schematic of the solar cell after assembly. The orange square is the sensitized film on the white FTO piece. The grey frame is the surlyn frame and the white square with the hole (being on top of the other white glass piece) is the counter electrode.

Three different electrolyte solutions, I^-/I_3^-, Co^{2+}/Co^{3+} and Co^{2+}/Co^{3+} + TPAA were prepared in MeCN according to the concentrations in Table 7.5 and 7.6. Cells were filled with an electrolyte by placing a drop of electrolyte on the hole in the counter electrode and then gently applying a vacuum to the cell in a desiccator. For cells with Pt counter electrode the electrolyte I^-/I_3^- was used, and for cells with PEDOT counter electrode either electrolyte Co^{2+}/Co^{3+} or Co^{2+}/Co^{3+} + TPAA were used. After filling, the cells were immediately wiped with acetone and sealed by placing a square of surlyn and a thin glass slide on top of the counter electrode hole and heating it with a soldering pen until the surlyn melted.

Table 7.5: Concentrations in MeCN for mixing the electrolyte I^-/I_3^-.

Compound \Electrolyte	I^-/I_3^-
Tetra-butyl-ammonium (mol/l)	0.6
LiI (mol/l)	0.1
I_2 (mol/l)	0.05
Tert-butyl-pyridine (mol/l)	0.2

Table 7.6: Concentrations in MeCN for mixing the electrolytes Co^{2+}/Co^{3+} and Co^{2+}/Co^{3+} + TPAA.

Compound \Electrolyte	Co^{2+}/Co^{3+}	Co^{2+}/Co^{3+} + TPAA
$LiClO_4$ (mol/l)	0.1	0.1
$Co(bpy)_3(PF_6)_2$ (mol/l)	0.22	0.22
$Co(bpy)_3(PF_6)_3$ (mol/l)	0.05	0.05
4-tert-butylpyridine (mol/l)	0.2	0.2
TPAA (mol/l)	0	0.1

To make better electrical contacts, parts of FTO sticking out were painted with silver-paint. The solar cells were now finished, see Figure 7.5. The different combinations of dye and electrodes tested are stated in Table 7.7. For all solar cells an IV-characteristics and IPCE were measured. For the best selected solar cells of each kind, the IV-characteristics were remeasured after one day.

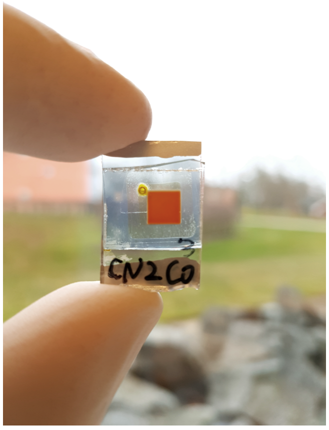

Figure 7.5: A finished DSSC fabricated in the solar cell labs at Physical Chemistry, Uppsala University.

Table 7.7: The different combinations of dye and electrolyte for which solar cells were fabricated.

Dye	Electrolytes		
	I^-/I_3^-	Co^{2+}/Co^{3+}	Co^{2+}/Co^{3+} + TPAA
FeCAB26		✓	✓
FeCABCN2	✓	✓	✓

To be able to perform transmission measurements such as photo-induced absorption, transparent full-cells were fabricated. The transparent full-cells were fabricated in exactly the same way as the real solar cells, except for that the scattering layer in Figure 7.3 was omitted. Transparent full-cells were fabricated for the dyes and electrolyte combinations seen in Table 7.8. For each transparent full-cell a placebo with inert electrolyte consisting of the same solution as the electrolyte without the active redox couple was fabricated.

Table 7.8: The different combinations of dye and electrolyte for which transparent full-cells were fabricated.

Dye	Electrolytes		
	I^-/I_3^-	Co^{2+}/Co^{3+}	Co^{2+}/Co^{3+} + TPAA
FeCAB26	✓		
FeCABCN2	✓		✓

7.7 Full-Cell Characterization

To measure the IV-characteristics of the solar cells, a solar simulator was used. Firstly, the lamp intensity in a specific spot at a fixed distance from the lamp was calibrated to give AM1.5. This was done by measuring the voltage over a calibration solar cell placed in that specific spot, that gave a known voltage when exposed to AM1.5. Then, the solar cell to be measured was put in a holder with the sensitized area facing towards the lamp. A rectangular mask in the holder made sure that only the sensitized area was exposed to light. The solar cell was contacted so voltage could be measured and applied. The holder was put in the specific point under the lamp and the open circuit voltage was measured. Depending on this value, a scan from -0.05 V to ~0.2 V above the V_{oc} was performed. From this, quantities like the conversion efficiency, the short circuit current density and fill factor were calculated. The first time the IV-characteristics were measured, all solar cells were measured two times; with and without a filter letting 10 % of the light through (simulating sunlight on a cloudy day). The filter was however not used the day after when the IV-characteristics of the best solar cells were remeasured to investigate if there had been any improvement.

To measure the IPCE, the setup in Figure 6.14 was used. The sample was mounted in a holder with the active area of the solar cell facing the light and selected by a rectangular mask. The solar cell was connected to a multimeter so the photocurrent could be measured while the light was scanned from 330 nm to 800 nm in steps of 10 nm. Firstly, a calibration Si-solar cell with a known IPCE-curve was measured. For all solar cells, the photocurrent was measured in the same way and then by the software converted to an IPCE-curve from the calibration curve.

For the transparent solar cells, photon induced absorption (PIA) was measured, see setup in Figure 6.15. The transparent cells were mounted in a holder with a rectangular mask, leaving the light to only pass through the sensitized area. The sample was excited by a laser diode at 470 nm and with a repetition rate of 9.33 Hz. The PIA spectra were all sampled in the region 500 nm to 1000 nm in steps of 10 nm. The spectra of transparent cells with the same dye with electrolyte and with inert electrolyte were plotted together to see the difference.

7.8 DFT Calculations

DFT-calculations were carried out to optimize the ground state geometry of a molecule of given charge and spin. Firstly an initial guess of the geometries for FeCAB26, the ligand of FeCAB26 and FeCABCN2 were constructed in the program "Gaussian". The overall ground state geometries were then optimized by DFT calculations in Gaussian, using the basis set B3LYP* and the model 6-311G(d, p) in MeCN. After having the overall ground state geometry, other optimized local ground state geometries were calculated by giving the overall ground state geometry as an initial guess but changing the charge and spin. If a calculation did not succeed, parameters like the calculation time, the amount of memory per core, the initial geometry guess and the largest allowed step in energy were changed. If a calculation was successful, the calculation output was assigned an electronic state and the energy of the state, the average Fe-ligand bond length and the spin density distribution over the molecule were obtained. All geometries optimized and their assigned states are given in Table 7.9.

Table 7.9: All combinations of spin and charge that an optimized geometry was calculated from for each molecule. For those calculated, the table states which state was assigned to the calculated optimized geometry.

Spin & Charge	**^{1}Fe(II)**	**^{3}Fe(II)**	**^{2}Fe(III)**	**^{2}Fe(I)**	**^{3}Fe(II)**	**^{5}Fe(II)**
FeCAB26	GS	^{3}MLCT	ox GS	red GS	^{3}MC	^{5}MC
FeCAB26 ligand	GS	triplet				
FeCABCN2	GS	^{3}MLCT	ox GS	red GS	^{3}MC	^{5}MC

Since two states have the same spin and charge, namely the ^{3}MLCT-state and the ^{3}MC-state, special care was taken to really identify which one had been calculated. The states were assigned according to their Fe-ligand average bond length and the spin density (especially Mulliken spin density on Fe). For both FeCAB26 and FeCABCN2 it turned out that the overall ground state geometry as initial guess yielded the ^{3}MLCT-state. To find the ^{3}MC-state, the optimized ^{5}MC-state geometry was sent in as an initial guess (since the geometries for these states are similar). For all optimized geometries the spin density was calculated and imaged. For the overall ground states, also selected molecular orbitals were imaged.

To be able to simulate absorption spectra for the different molecules, singlet to singlet excitations from the ground state were calculated by TD-DFT. For FeCAB26 the 40 first excitations were successfully calculated, for the ligand of FeCAB26 and FeCABCN2 the 30 first were successfully calculated. From these calculations, absorption spectra were simulated in Matlab by giving each transition a gaussian function scaled with the oscillator strength and adding them. The FMHW used for the gaussian functions were 10 nm for FeCAB26 and FeCABCN2 and 5 nm for the ligand of FeCAB26 (since the ligand absorption is at shorter wavelengths and 10 nm comprised a too large energy width at that wavelengths).

8 Results & Analysis

8.1 Steady-State Absorption

In this thesis, three different samples were investigated through steady-state spectroscopy: FeCAB26, the ligand of FeCAB26 and FeCABCN2. It turned out that the complexes FeCAB26 and FeCABCN2 required different methods of analysis. Since FeCAB26 is homoleptic it was easier to investigate how the pure ligand features influenced the characteristics of the full complex compared to the heteroleptic FeCABCN2. For FeCABCN2, instead special analysis of the stability was needed.

The extinction coefficients were measured and calculated for the samples stated in Table 7.2 according to the procedure outlined in section 7.1, and the results are presented in Figures 8.1-8.3. In the graphs the extinction coefficient is given with standard error bars from the linear fit at each wavelength.

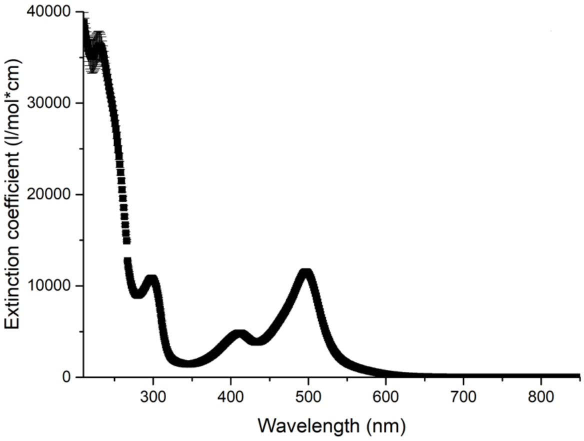

Figure 8.1: Extinction coefficient for FeCAB26 plotted as a function of wavelength. Error bars reflecting the standard error of the linear fit are included in the graph.

The peaks in the extinction coefficient of FeCAB26 (Figure 8.1) are (from right to left) at 495 nm, 411 nm, 298 nm and 231 nm. Within this sort of transition-metal complexes the peaks 495 nm and 411 nm, plus the band they make up, is usually characterized as a charge-transfer band i.e. absorption to MLCT-states. The absorption band looks similar to earlier in-house molecule charge-transfer bands, for example the related complex FeCABC1 in [7], and have an extinction coefficient of the same order of magnitude. The peaks at 298 nm and 231 nm however, are thought to arise from ligand-centred excitations i.e. from a ligand π-state to a ligand π^*-state. To try and verify this, the extinction coefficient of the pure FeCAB26 ligand was measured (and calculated), see Figure 8.2.

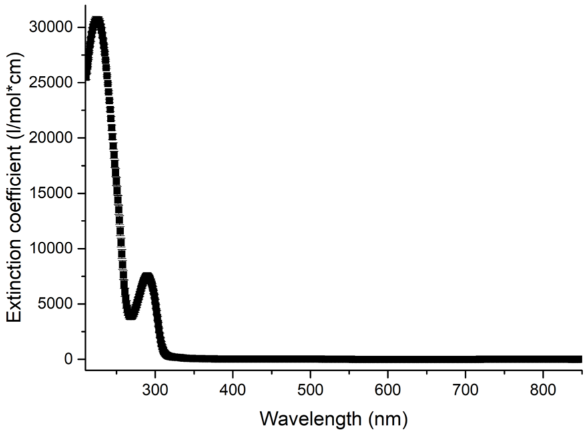

Figure 8.2: Extinction coefficient for the ligand of FeCAB26 plotted as a function of wavelength. Error bars reflecting the standard error of the linear fit are included in the graph.

The peaks in the extinction coefficient of the ligand of FeCAB26 (Figure 8.2) are (from right to left) at 290 nm and 224 nm. The spectrum in Figure 8.2 looks similar to the spectrum in Figure 8.1 below 350 nm, with the two sets of peaks differing in position less than 10 nm. This strongly indicates that the extinction coefficient of FeCAB26 below 350 nm consists of contributions almost only from its ligands. The fact that the two sets of peaks are not at exactly the same positions are expected since the free ligand is protonated and thus does not have exactly the same structure as the ligands bound to iron. Also, the ligand orbitals do mix with the metal orbitals to some extent.

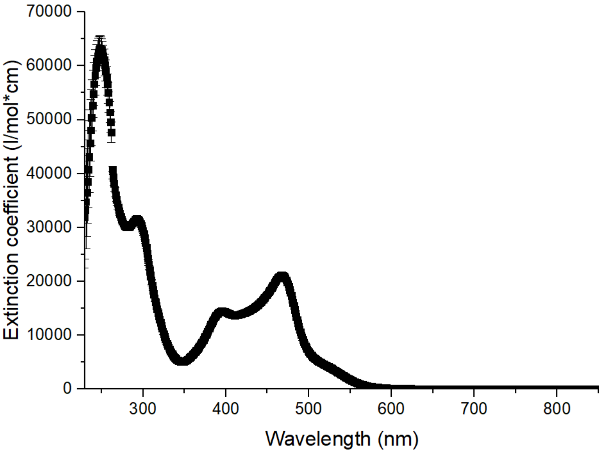

Figure 8.3: Extinction coefficient for FeCABCN2 plotted as a function of wavelength. Error bars reflecting the standard error of the linear fit are included in the graph.

The peaks in the extinction coefficient of FeCABCN2 (Figure 8.3) are (from right to left) at 520 nm (shoulder), 468 nm, 395 nm, 292 nm and 248 nm. The extinction coefficient of FeCABCN2 looks similar to the extinction coefficient of FeCAB26 regarding the main features, a charge-transfer band around 400 nm to 500 nm and then contributions from ligand absorption at shorter wavelength and higher extinction coefficient. However, a feature not present in the absorption spectrum in Figure 8.10 a around 520 nm is seen. To further investigate the origin of this feature, absorption spectra for a range of concentrations used in the extinction coefficient measurement are plotted together in Figure 8.4, normalized to 1 at 470 nm.

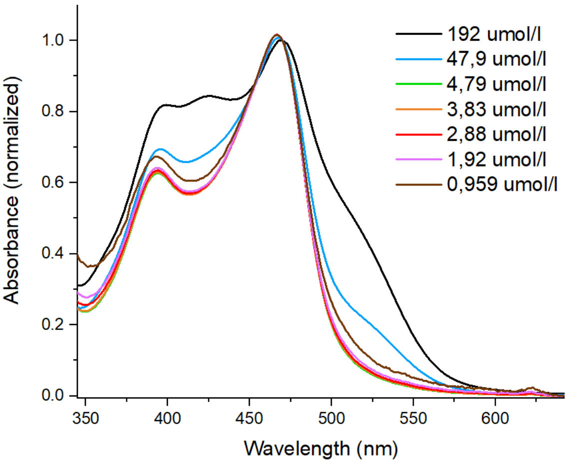

Figure 8.4: The absorption spectra used to calculate the extinction coefficient of FeCABCN2, with given concentrations. All spectra are normalized to 1 at 470 nm to be able to compare features.

As can be seen in Figure 8.4, the extra peak at 426 nm and the shoulder around 520 nm can be seen for the highest concentrated solution and also (but more weakly) for the second highest concentration. Since absorption is a linear process, a true absorption peak should not change its relative intensity to another peak. Instead the extra features could be due to agglomeration of the complex in MeCN. This would explain why the features disappear as the sample is diluted. To further elaborate on this, the stability of the FeCABCN2 absorption spectrum was investigated.

In Figure 8.5 a, the absorption spectra from the same sample of FeCABCN2 measured over a series of days by procedure described in section 7.2 are plotted. As can be seen in the graph, the absorbance changes during the days in a continuous way. Compared to the absorption spectrum of lower concentration (Figure 8.5 b), the spectral shape and number of peaks are different (to compare the OD between these two graphs, the stability absorption spectra should be multiplied by 10 since they were measured in a cuvette 10 times as thin).

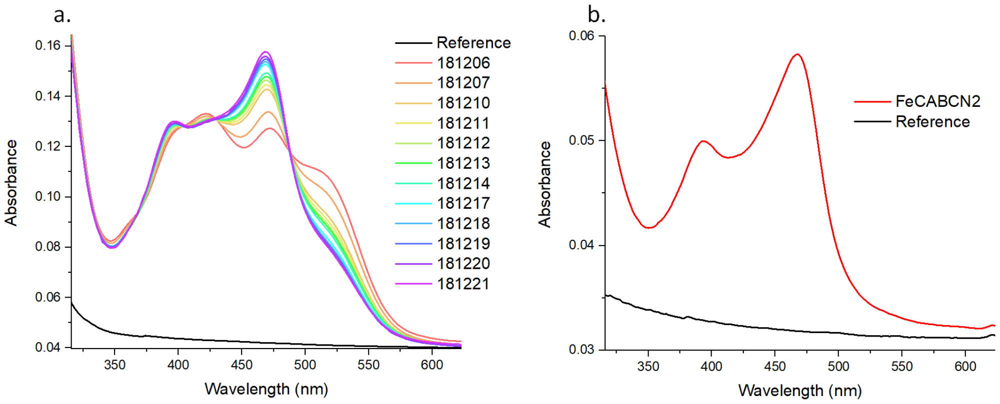

Figure 8.5: a, the absorption spectra measured during two weeks to see the stability of FeCABCN2. b, the absorption spectrum measured for the sample of FeCABCN2 used for the excitation spectra measurements.

The same extra features as seen in the extinction coefficient measurement (Figure 8.3), the extra peak at 426 nm and the shoulder around 520 nm, are seen also in this spectrum. With time, they actually both decrease while the "true" peaks increase (mainly the peak at 468 nm). This further strengthens the theory of agglomeration. In the beginning the highly concentrated FeCABCN2 might not fully dissolve and the agglomerates give features in the absorption, but with time the agglomerates slowly split up and the spectra approaches the spectrum for low concentration (Figure 8.5 b). Agglomeration also seems like reasonable phenomenon for a molecule having one partly positive and one partly negative side.

8.2 Steady-State Emission

The emission for both complexes and the ligand of FeCAB26 were also probed, since emission offers information about the lifetime of the excited states. The system needs to stay in the excited state for some time for the spontaneous emission to happen, thus it is a sign of not only ultrafast decay which is good for dyes in DSSC:s. In this case it is the lifetime of the ^{3}MLCT-state that is of interest, so the emission should come due to absorption in the charge-transfer band. Since all emission is Stokes' shifted it should have longer wavelength than the charge-transfer band. Excitation spectra are used to deem where potential peaks in the emission spectra arise from. Since the excitation spectrum gives emission intensity at a certain probed wavelength (the wavelength of the selected peak in the emission spectrum) as a function of excitation wavelength, the intensity should depend linearly to how much is absorbed at each excitation wavelength. Thus, the excitation spectrum should ideally have the same shape as the absorption spectrum of the sample in the region where light resulting in the emission is absorbed. This is, however, not a strict rule that can be used to fully asses whether a peak in an emission spectrum comes from true emission or is an artefact.

In Figure 8.6 b, all emission spectra measured for FeCAB26 have been put together to get a full characterization of the emission of the compound in the wavelength range 300-900 nm. Artefacts such as Raman peaks have been removed together with parts where the reference intensity was higher than the sample intensity.

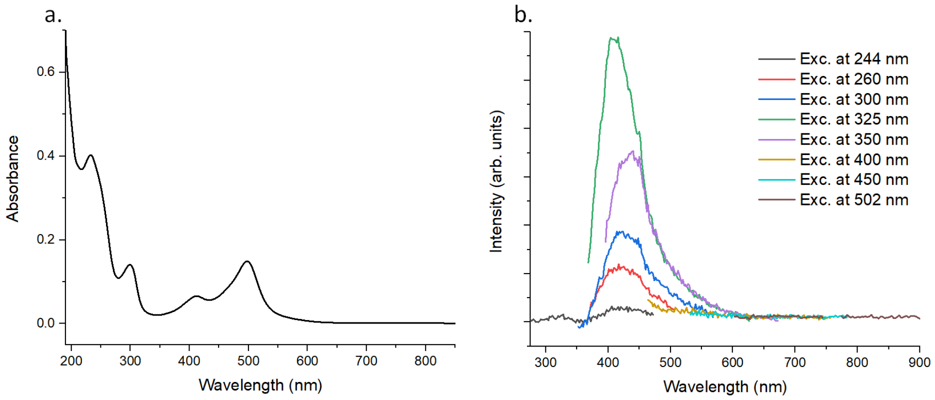

Figure 8.6: a, the absorbance of the solution measured on. b, emission intensity for FeCAB26 plotted as a function of wavelength.

One peak around 425 nm was clearly identified for several of the different excitations and was further investigated by taking an excitation spectrum, Figure 8.7.

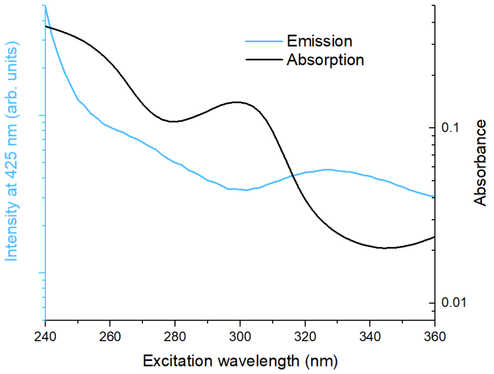

Figure 8.7: Emission intensity at 425 nm for FeCAB26 plotted as a function of excitation wavelength. No reference measurement of this excitation spectrum was measured and it is thus not removed. The absorbance of the sample is included in the graph on a linked wavelength scale but with a separate absorbance axis. The intensity and the absorbance are plotted in logscales to better compare the changes in the data.

In Figure 8.6 b, it looks like there is emission at around 425 nm. This emission however has a very small Stokes' shift to come from the charge-transfer band of FeCAB26 (compare with the absorption spectrum in Figure 8.6 a). The excitation spectrum at 425 nm, Figure 8.7, in this case does not clarify whether the emission is caused by the ligand state or not. When the emission intensity does not follow the absorbance, as in Figure 8.7, no conclusion can be drawn. Also, to really be able to say something from Figure 8.7 it would be the best to also have measured the excitation spectrum of MeCN as a reference.

To better understand the origin of the emission for FeCAB26, Figure 8.6 b should be compared with the emission of the pure ligand, also in MeCN, Figure 8.8 b. All emission spectra were measured with the same settings as for FeCAB26. The graph was constructed in the same way as for FeCAB26.

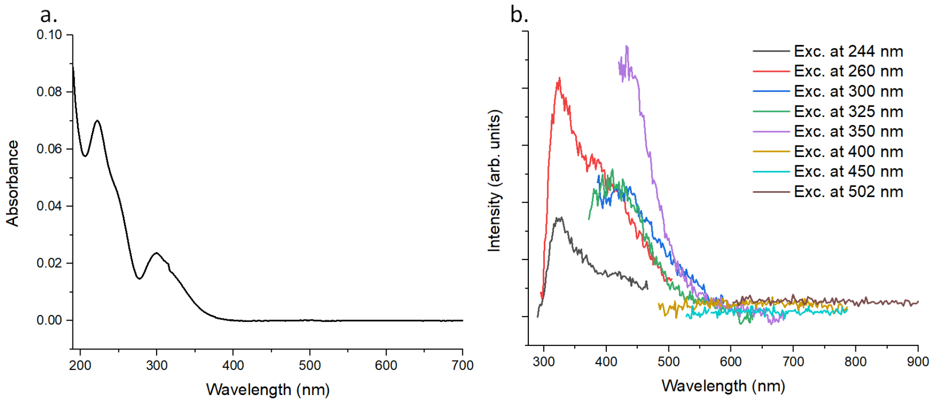

Figure 8.8: a, the absorbance of the measured solution. b, emission intensity for the ligand of FeCAB26 plotted as a function of wavelength.

In Figure 8.8 b two possible peaks were identified at 425 nm and 320 nm. Excitation spectra were measured at both wavelengths, see Figure 8.9.

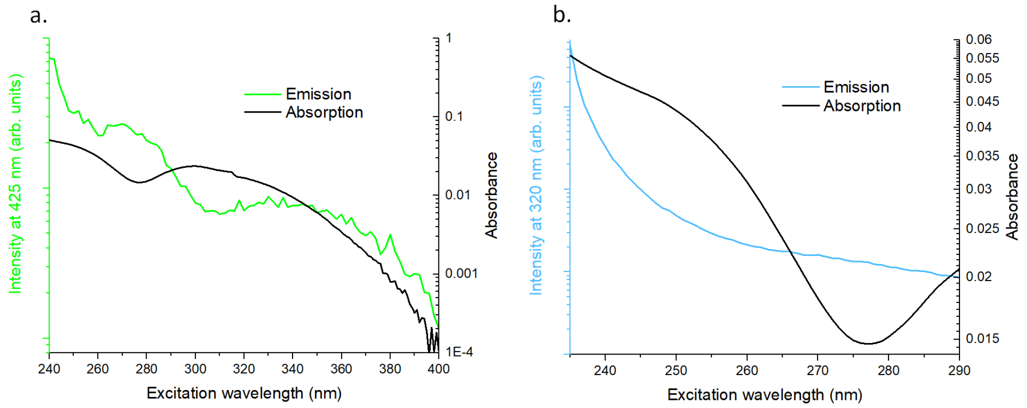

Figure 8.9: Emission intensity at a 425 nm and b 320 nm for the ligand of FeCAB26, plotted as a function of excitation wavelength. In a, a reference excitation spectra of MeCN has been removed from the data. In b, no reference has been removed. The absorbance of the sample is always included in the graphs on a linked wavelength scale but with a separate absorbance axis. The intensity and the absorbance are plotted in logscales to better compare the changes in the data.

For the ligand of FeCAB26 two potentially emissive wavelengths have been investigated: namely 425 nm and 320 nm. The peak at 425 nm is thus present in emission spectra both from the full complex FeCAB26 and from its ligands. In the excitation spectrum in Figure 8.9 a, the emission intensity partially follows the absorbance, which suggests potential true emission. Due to this excitation spectrum and the fact that the emission peak is visible both for the full complex FeCAB26 and for the ligand, the peaks at 425 nm are probably due to emission from the FeCAB26 ligand (the fact that the peak is more intense for the 350 nm excitation wavelength is due to the fact that a Raman peak in MeCN was accidentally excited). The peak at 320 nm is there for two excitation wavelengths, but no conclusions can be drawn from the excitation spectrum in Figure 8.9 b since it does not follow the absorbance and no reference measurement was made to verify.

In Figure 8.10 b, all emission spectra measured for FeCABCN2 have been put together to get a full characterization of the emission of the compound in the wavelength range 330-850 nm. The graph was constructed in the same way as for FeCAB26.

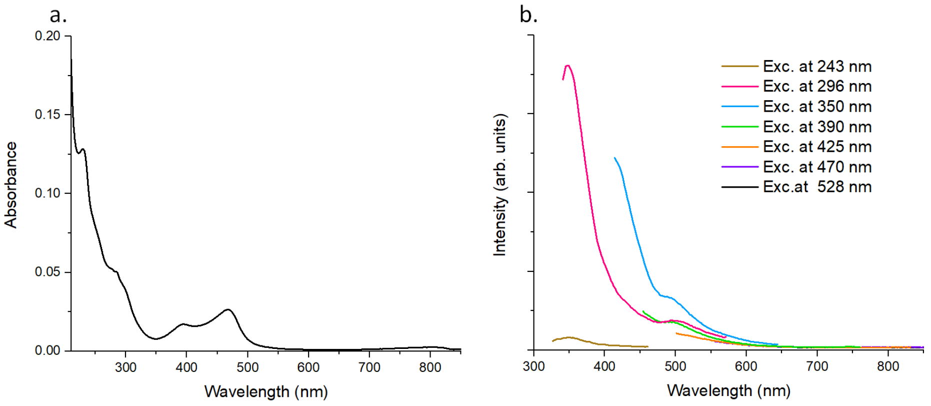

Figure 8.10: a, the absorbance of the solution used to measure excitation spectra. b, emission intensity for FeCABCN2 plotted as a function of wavelength. Note that the solution of FeCABCN2 used to measure the spectrum in b was more highly concentrated, but had the same spectral features in the absorption spectrum as the absorption spectrum of lower concentration (a).

In Figure 8.10 b, two possible emission peaks were identified around 500 nm and 350 nm. To further investigate this, excitation spectra were measured for these two wavelengths, as shown in Figure 8.11.

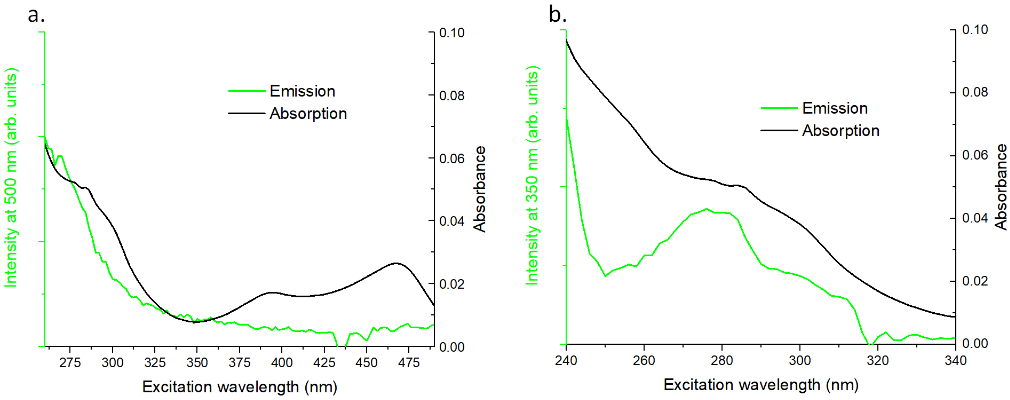

Figure 8.11: Emission intensity at a 500 nm and b 350 nm for FeCABCN2, plotted as a function of excitation wavelength. For both spectra a reference excitation spectra of MeCN has been removed from the data. The absorbance of the sample is always included in the graphs on a linked wavelength scale but with a separate absorbance axis.

The excitation spectra, Figure 8.11, suggest that these two peaks at 500 nm and 350 nm potentially correspond to true emission of the complex since both spectra follow to some extent the absorbance. However, it is clear that the emission, if it is real, must come from the ligands of FeCABCN2, since the part of the absorbance the excitation spectra follow is the ligand absorbance.

Can emission really come from the ligand part of the complexes, even though this does not obey Kasha's rule? Exceptions to Kasha's rule do exist (see for example [40]) and in the complexes there are molecular orbitals with almost no contribution from the iron-centred orbitals. The ligands could in a way be an autonomous system that can absorb and emit photons without hardly involving the iron. Also, the complexes experience ultra-fast intersystem crossing from the ^{1}MLCT-state to the ^{3}MLCT-state, leaving them in a state from where emission is not classically allowed. The answer to the question is not yet known, but the state of the art iron-complexes investigated in this thesis would be far from the first molecules not obeying Kasha's rule. However, the rather unusual behaviour will be definitely point of further investigations but goes beyond the scope of this thesis.

8.3 Transient Absorption

One of the main goals of this thesis is to investigate if the complexes FeCAB26 and FeCABCN2 are promising for use as sensitizers in DSSC:s. To do this, not only the steady-state properties are a key part, but also the excited state properties should be investigated. Lifetimes of different excited states and their relaxation pathways come into play when investigating if a dye can inject electrons into the conduction band of TiO_2. Therefore, TA measurements were performed for both complexes sensitized on TiO_2 mimicking the DSSC (but with no electrolyte as dye regeneration by electrolyte is mostly diffusion driven, thus happening on the ms-timescale, the presence of electrolyte is unlikely to change the observed ps-ns dynamics of the dye), and sensitized on Al_2O_3 to get a reference since electrons can not be injected into the Al_2O_3 conduction band. Also, TA measurement were performed for the dyes in solution of MeCN to be able to compare the behaviour of the dyes in solution and on films. Samples for TA measurements were prepared according to the procedure described in section 7.4 and TA measurements were performed according to the procedure described in section 7.5

In Figure 8.12, the measured, fitted TA data from (a-b) FeCAB26 in MeCN (1 mm cuvette), (c-d) sensitized on TiO_2 encapsulated in MeCN and (e-f) sensitized on Al_2O_3 encapsulated in MeCN are shown. For the TA kinetics, the plotted wavelengths are selected according to interesting points in the absorption spectrum of FeCAB26 (Figure 8.6 a). The data is cut to remove scatter from the pump beam. Since investigation of any eventual ultrafast (sub-ps) processes is not relevant for the purposes of this thesis, in all datasets times shorter than ~500 fs are omitted.

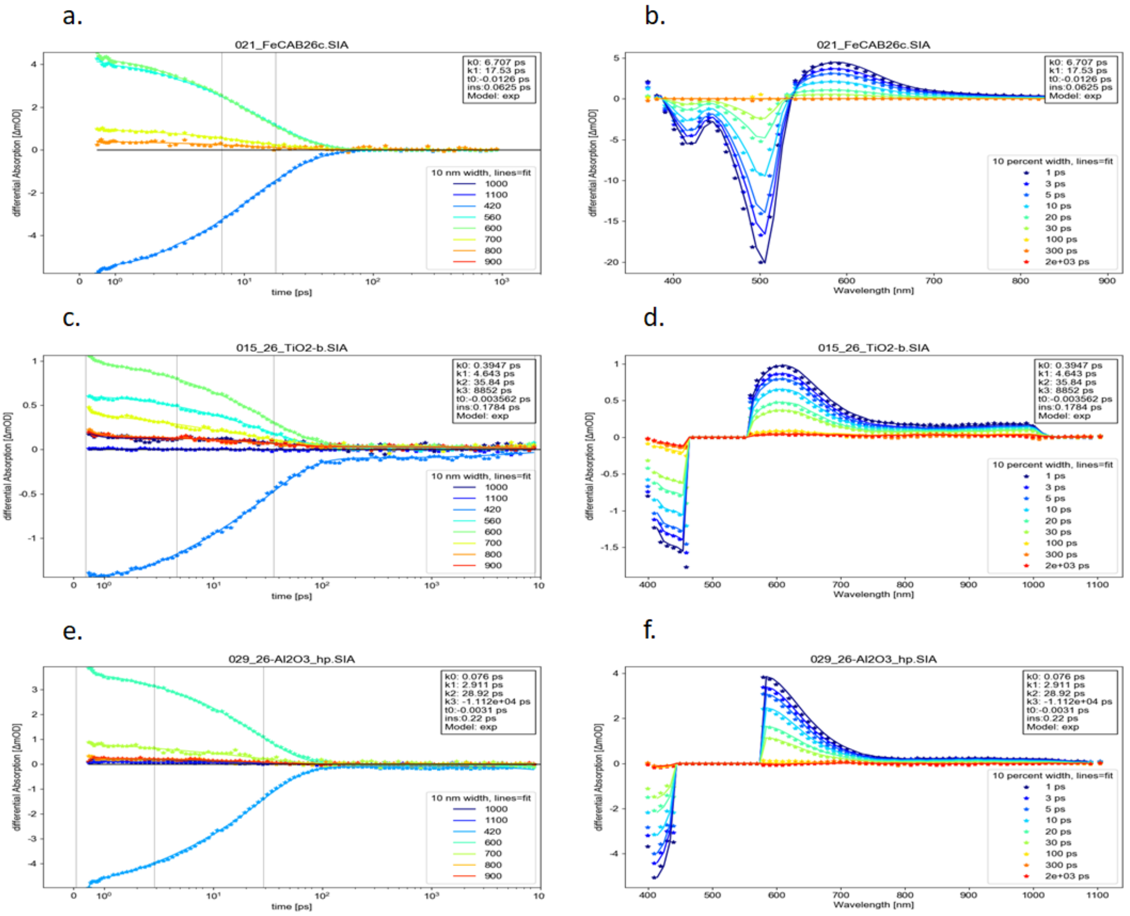

Figure 8.12: Fitted TA data measured for a-b FeCAB26 in MeCN (1 mm cuvette), c-d sensitized on TiO_2 encapsulated in MeCN and e-f sensitized on Al_2O_3 encapsulated in MeCN. To the left are the TA kinetics and to the right are the TA spectra.

The lifetimes τ of the fitted exponentials are given in Table 8.1.

Table 8.1: Table containing the lifetimes τ from the fitted exponentials for the TA data measured for FeCAB26 shown in Figure 8.12.

Sample	τ_1 **(ps)**	τ_2 **(ps)**	τ_3 **(ps)**	τ_4 **(ns)**
FeCAB26 in MeCN	6.7	17.5	-	-
FeCAB26 on TiO_2	0.4	4.6	35.8	8.9
FeCAB26 on Al_2O_3	0.08	2.9	28.9	-11.1

In the TA spectrum for FeCAB26 in MeCN (Figure 8.12 b), a fully developed ground state bleach reflecting exactly the peaks in the absorption spectrum (Figure 8.6 a) is seen. The positive signal in the TA spectrum is an excited state absorption. Both signals decay at the same rate and after 300 ps the TA signal in the spectrum and in the kinetic (Figure 8.12 a) decays completely. This indicates that no other processes than ground state absorption, excited state absorption and relaxation back to the ground state have occurred. The fitted lifetime of 17.5 ps corresponds to the relaxation of the excited state back to the ground state, since there are no competing processes, see the left panel of Figure 8.13.

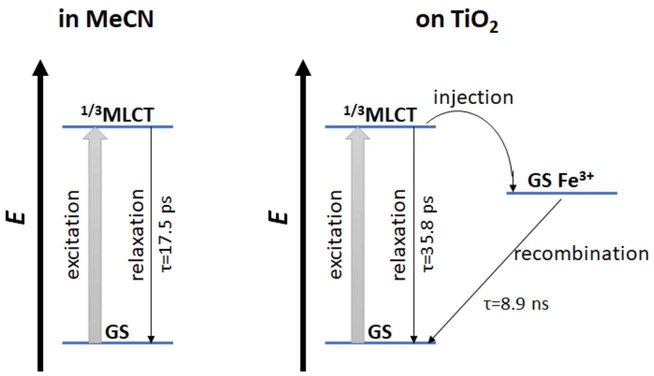

Figure 8.13: A simplified schematic of selected processes taking place during the TA measurement for FeCAB26 in MeCN and sensitized on TiO_2, with assigned fitted lifetimes.

The TA data from FeCAB26 sensitized on TiO_2 (Figure 8.12 c-d) show the same GSB and ESA features as the FeCAB26 in MeCN spectrum even though parts are cut out due to scattering. However, there is also a long-lived component, fitted to a lifetime of 8.9 ns, that does not decay to zero during the timescale of the measurement. When looking closely at the TA spectra in Figure 8.12 b and d, one can also see that at 300 ps spectrum b is flat whereas d is not. In d, the GSB signal has not decayed to zero while the ESA basically is zero, indicating that more electrons are absorbed from the ground state than is relaxing back to the ground state. This is a strong indication that electron injection into the conduction band of TiO_2 has occurred. To also see the absorption of the oxidized dye as a positive signal instead of ESA would be further proof of the injection, and from the PIA measurement in Figure 8.22 it can be seen that that the oxidized dye absorbs around 520 nm to 700 nm. It is thus likely that the small positive signal in the TA spectrum at 100 ps is indeed not ESA but a weak oxidized dye spectrum. Although the data quality does not allow unambiguous identification of the oxidized dye spectrum, the long-lived component is a solid signature of the electron injection into the conduction band of TiO_2. The fitted component at 35.8 ps is the only one of the same order of magnitude as the relaxation lifetime in MeCN, thus this is probably the relaxation lifetime from excited state to ground state. Important process with lifetimes are illustrated in the right panel of Figure 8.13.

The TA data of FeCAB26 sensitized on Al_2O_3 (Figure 8.12 e-f) is similar to the data of FeCAB26 in MeCN (except the scatter-cut region in the TA spectra). The data is not expected to show a long-lived component since electrons can not be injected into the conduction band of Al_2O_3. One relaxation lifetime of 28.9 ps and one long-lived growing component of lifetime 11.1 ns were fitted to the data. When looking at the TA kinetic (Figure 8.12 e), no clear growing long-lived component is seen. In the data analysis, an incorrect chirp-correction can cause the zero baseline to be at different levels for some of the wavelengths. This is the case here and the fitting assigns this as a growing long-lived component (more discussion about this together with Figure 8.16).

In Figure 8.14, the measured, fitted TA data from (a-b) FeCABCN2 in MeCN (1 mm cuvette), (c-d) sensitized on TiO_2 encapsulated in MeCN and (e-f) sensitized on Al_2O_3 encapsulated in MeCN are shown. For the TA kinetics, the plotted wavelengths are selected according to interesting points in the absorption spectrum of FeCABCN2. The data is cut to remove scatter from the pump beam. Since investigation of any eventual ultrafast (sub-ps) processes is not relevant for the purposes of this thesis, in all datasets times shorter than ~500 fs are omitted.

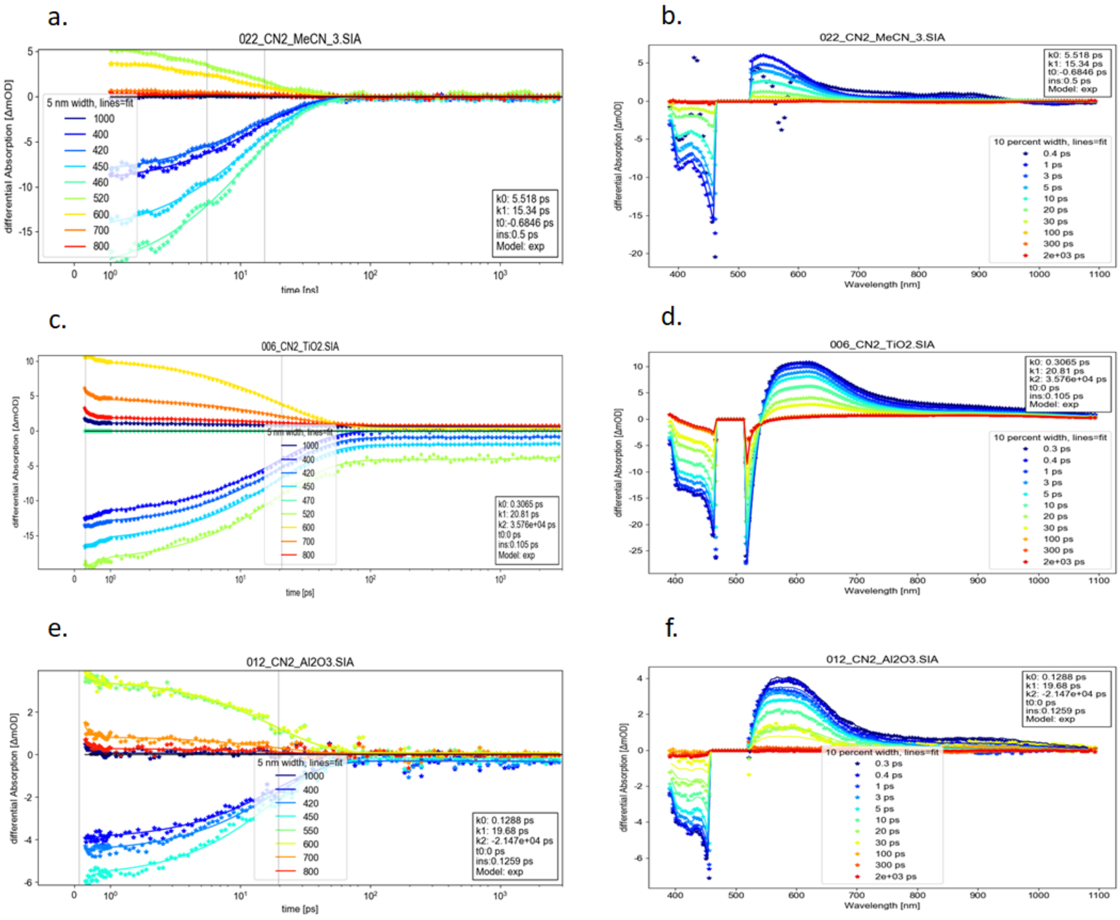

Figure 8.14: Fitted TA data measured for a-b FeCABCN2 in MeCN (1 mm cuvette), c-d sensitized on TiO_2 encapsulated in MeCN and e-f sensitized on Al_2O_3 encapsulated in MeCN. To the left are the TA kinetics and to the TA right are the spectra.

The lifetimes τ of the fitted exponentials are given in Table 8.2.

Table 8.2: Table containing the lifetimes τ from the fitted exponentials for the TA data measured for FeCABCN2 shown in Figure 8.14.

Sample	τ_1 **(ps)**	τ_2 **(ps)**	τ_3 **(ns)**
FeCABCN2 in MeCN	5.5	15.3	-
FeCABCN2 on TiO_2	0.3	20.8	35.8
FeCABCN2 on Al_2O_3	0.1	19.7	-21.5

The TA data of FeCABCN2, Figure 8.14 has very similar features as the data of FeCAB26, but has a worse signal-to-noise ratio. Therefore the already non-trivial chirp-correction became very complicated for this dataset which means that small deviations of the baseline are probably due to this rather than real effects. The baseline subtraction uncertainty is demonstrated in the TA spectrum of FeCABCN2 in MeCN (Figure 8.14 b), but in the TA kinetic (Figure 8.14 a) it is rather clear that all signals decay to zero. The fitted lifetime of 15.3 ps is assigned to the relaxation from the first excited state to the ground state, see the left panel of Figure 8.15.

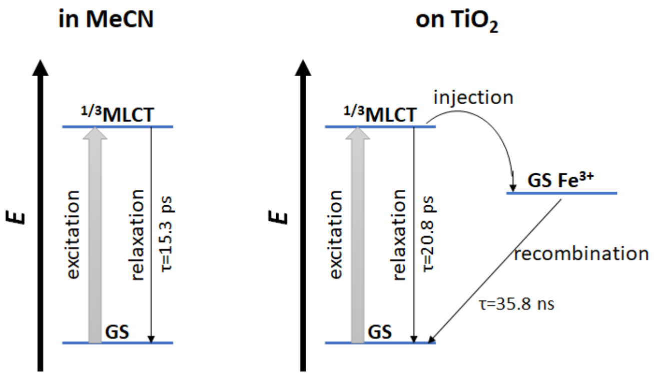

Figure 8.15: A simplified schematic of selected processes taking place during the TA measurement for FeCABCN2 in MeCN and sensitized on TiO_2, with assigned fitted lifetimes.

In the TiO_2 data there is a clear long-lived component that can be seen easily in the TA kinetic (Figure 8.14 c) and also in the TA spectrum (Figure 8.14 d) since at 300 ps the ESA signal but not the GSB signal has fully decayed. This strongly indicates that there is injection into the conduction band of TiO_2. From the PIA measurement in Figure 8.22, a potential oxidized dye spectrum absorbs between 600 nm and 1000 nm. This would correspond to a very broad positive feature in the TA spectra (Figure 8.14 d) that is not seen, and can thus not further confirm the injection. The long-lived component, fitted with a lifetime of 35.8 ns, is however sufficient indication of injection since it is very clearly seen in the TA kinetic (Figure 8.14 c). The 20.8 ps component is assigned as the relaxation lifetime due to it being of the same order of magnitude as the relaxation lifetime in MeCN, see the right panel of Figure 8.15.

Since the TA kinetic of FeCABCN2 sensitized on Al_2O_3 (Figure 8.14 e) do not decay fully to zero for long times, it looks like there is a long lived component. To this component a lifetime of -21.5 ns is fitted, suggesting a growth over time. This is however not the case. Since no pre-zero timescale was included in the fit the raw data of the TA kinetic is shown in Figure 8.16. As can be seen in Figure 8.16, the pre-zero difference absorbance is on the same level as the long lived component (for each particular wavelength), which means the long-lived component is on the true zero level. Thus the growing, long-lived component is an artifact due to not fully corrected background and chirp. The 19.7 ps component is assigned as the relaxation lifetime since it is on the same order of magnitude as previously assigned relaxation lifetimes of FeCABCN2.

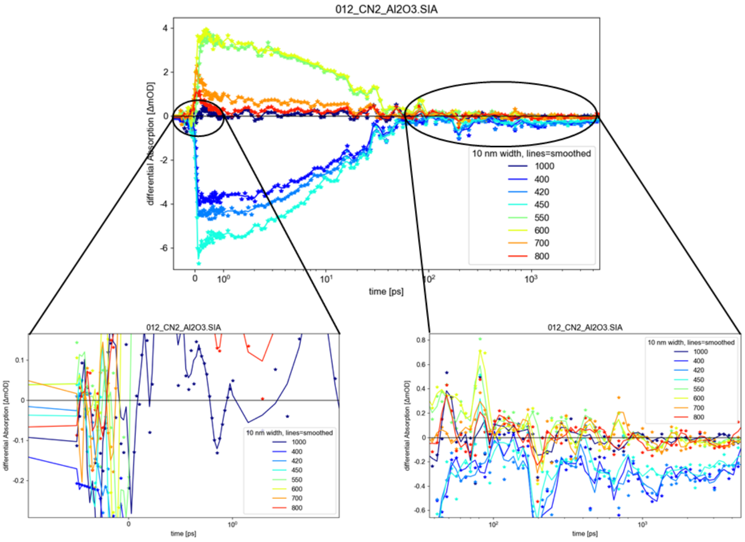

Figure 8.16: Raw TA kinetic data measured for FeCABCN2 sensitized on Al_2O_3 encapsulated in MeCN. The zoom shows the level of the difference absorbance prezero in time and at long timescale.

To almost all TA data more decay components have been added to make the fit more consistent with the data, see Tables 8.1 and 8.2. The components on the 1 ps order represent likely thermal cooling of the excited molecules. Since this decay channel contributes only marginally to the observed excited state dynamics (and thus DSSC performance), it is not considered to be within the scope of this thesis. The sub-ps components are too fast to be well resolved within the measurements performed, and are therefore also not further discussed.

8.4 Full-Cell Characterization

Steady-state and ultrafast properties have been investigated within the part of the goal to understand the fundamental molecular properties. But to understand how these properties influence the photo-induced electronic properties, which is the second part of the goal, one needs to build full solar cells and measure the electronic characteristics. Building a DSSC is a very sensitive process which contains almost a large number of alternative ways and parameters to change. The group of Gerrit Boschloo at Uppsala University is working with optimizing this process for working DSSC dyes. This thesis is more aimed towards investigating whether the synthesized complexes can work as sensitizers in DSSCs. Therefore, during the week of work conducted in Uppsala the goal was to show a proof of concept rather than optimizing the DSSCs, a process taking an average of three months work for a skilled person in the group of Boschloo. Solar cells were built according to the procedure in section 7.6 and characterized according to the procedure in section 7.7.

Three different electrolytes were tested in the fabricated DSSCs: I^-/I_3^-, Co^{2+}/Co^{3+} and Co^{2+}/Co^{3+} + TPAA. The redox potentials of the oxidized dyes were estimated from DFT calculated ground state energies, see Table 8.5, to verify that the electrolytes were able to regenerate the dyes. In Figure 8.17 it is seen that all electrolytes should probably work for both dyes. There is however also the aspect of whether the electrolyte is capable of regenerating the oxidized dye fast enough, before recombination occurs. TPAA is an additive that has been shown by the Boschloo group to diminish recombination.[36] Therefore both Co^{2+}/Co^{3+} and Co^{2+}/Co^{3+} + TPAA electrolytes are investigated, but also the classical electrolyte I^-/I_3^- used for many DSSCs.

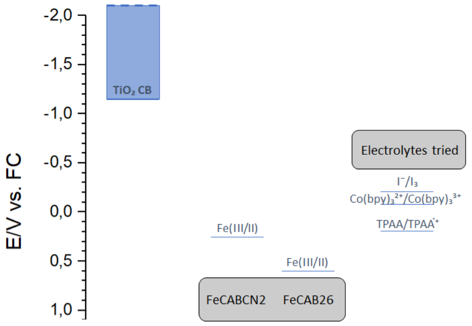

Figure 8.17: Schematic of the redox potentials of the dyes (estimated from DFT calculations) and the redox levels of the electrolyte (from [36]), also with the TiO_2 conduction band edge indicated.

For FeCAB26, four solar cells were fabricated; two with electrolyte Co^{2+}/Co^{3+} and two with electrolyte Co^{2+}/Co^{3+} + TPAA as seen in Table 8.3. In Table 8.3 also the characteristic parameters calculated from the IV-measurement and the IPCE-measurement are stated.

Table 8.3: Characteristics obtained from IV-measurement and IPCE-measurement of FeCAB26.

Cell name	Electrolyte	*η* (%) AM1.5	*Voc* (V)	*Jsc* (mA/cm²)	*FF*	*IPCE* (%) at 465nm	*η* (%) filter	*Voc* (V)	*Jsc* (mA/cm²)	*FF*
26 Co 1	Co^{2+}/Co^{3+}	0.0279	0.405	-0.131	0.526	noise	0.0280	0.345	-0.0167	0.485
26 Co 2	Co^{2+}/Co^{3+}	0.0255	0.420	-0.124	0.489	noise	0.0221	0.340	-0.0162	0.400
26 Co+ 1	Co^{2+}/Co^{3+} TPAA	0.0248	0.425	-0.113	0.515	noise	0.0217	0.350	-0.0152	0.408
26 Co+ 2	Co^{2+}/Co^{3+} TPAA	0.0231	0.410	-0.118	0.478	noise	0.0179	0.305	-0.015	0.392

In Figure 8.18 the individual IV-curves for all FeCAB26 solar cells are plotted. For comparison, the IV-curves at AM1.5 and with the 10 % filter are plotted together.

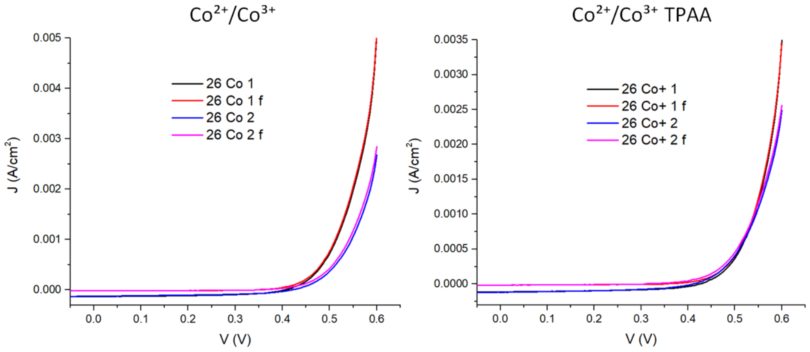

Figure 8.18: IV-curves from all solar cells of FeCAB26. f stands for filter.

In Figure 8.19 the measured IPCE is plotted as a function of wavelength for all solar cells fabricated of FeCAB26.

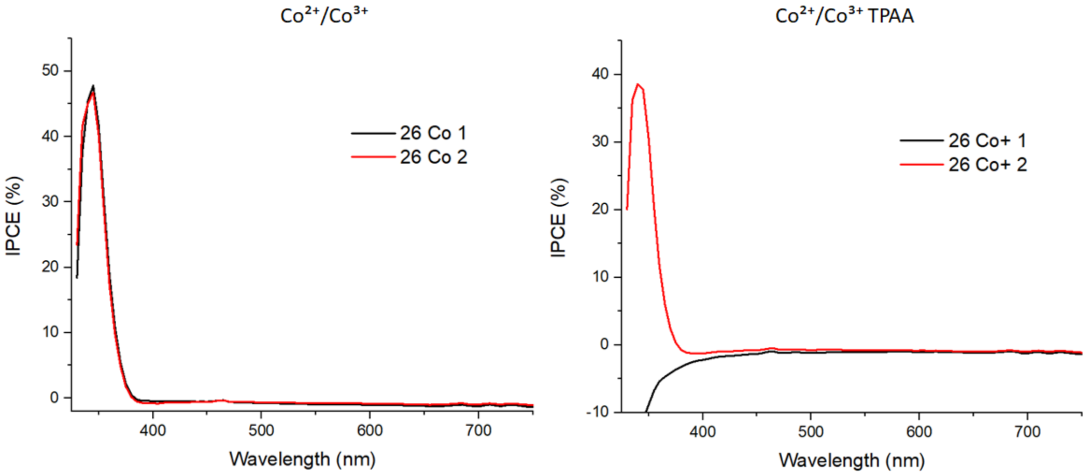

Figure 8.19: IPCE-curves from the solar cells of FeCAB26.

The DSSCs fabricated for FeCAB26 worked at best with a conversion efficiency of 0.028 %, see Table 8.3. However, the measured IV-curves in Figure 8.18 do show the typical IV-characteristic for a solar cell as in Figure 6.13 (the J-scale has the opposite sign convention as in Figure 6.13). TiO_2 itself can though work as a solar cell in a region around 340 nm where it absorbs, and at such low efficiencies it is hard to tell whether the photocurrent is generated by the dye or the titania. In the IPCE-measurements, Figure 8.19, all DSSCs yielded a non-measurable external quantum efficiency in the wavelength region where the dye should absorb. This indicates that the dye is not generating the photocurrent. For a good DSSC, the quantum efficiency coming from the dye should be significantly higher than the quantum efficiency coming from the titania, seen in the graphs as the peak at around 340 nm. The characteristic IV-curves thus probably only come from the titania energy-conversion which would explain why the solar cells are working at such a low conversion efficiency.

For FeCABCN2, seven solar cells were fabricated; one with electrolyte I^-/I_3^-, three with electrolyte Co^{2+}/Co^{3+} and three with electrolyte Co^{2+}/Co^{3+} + TPAA as stated in Table 8.4. In Table 8.4 also the characteristic parameters calculated from the IV-measurement and the IPCE-measurement are stated.

Table 8.4: Characteristics obtained from IV-measurement and IPCE-measurement of FeCABCN2. Rows coloured green denote the cells that were selected as the best ones of each kind.

Cell name	**Electrolyte**	***η* (%) AM1.5**	***Voc* (V)**	***Jsc* (mA/cm²)**	***FF***	***IPCE* (%) at 465nm**	***η* (%) filter**	***Voc* (V)**	***Jsc* (mA/cm²)**	***FF***	***η* (%) day 2**	***Voc* (V)**	***Jsc* (mA/cm²)**	***FF***
CN2 I	I^-/I_3^-	0.0731	0.430	-0.288	0.590	3.83	0.0780	0.370	-0.0337	0.626	0.116	0.445	-0.39	0.669
CN2 Co 1	Co^{2+}/Co^{3+}	0.0905	0.520	-0.288	0.604	2.73	0.0946	0.455	-0.034	0.610				
CN2 Co 2	Co^{2+}/Co^{3+}	0.0984	0.515	-0.319	0.599	3.57	0.112	0.455	-0.0384	0.644	0.103	0.515	-0.367	0.544
CN2 Co 3	Co^{2+}/Co^{3+}	0.0192	0.190	-0.296	0.341	2.45	0.0042	0.045	-0.0369	0.256				
CN2 Co+ 1	Co^{2+}/Co^{3+} TPAA	0.0816	0.520	-0.262	0.600	2.25	0.0828	0.455	-0.0318	0.572				
CN2 Co+ 2	Co^{2+}/Co^{3+} TPAA	0.0836	0.515	-0.268	0.606	1.94	0.0841	0.450	-0.032	0.584				
CN2 Co+ 3	Co^{2+}/Co^{3+} TPAA	0.105	0.545	-0.311	0.619	2.55	0.103	0.480	-0.0346	0.622	0.133	0.535	-0.375	0.664

In Figure 8.20 the individual IV-curves for the best selected FeCABCN2 solar cells of each kind are plotted. The IV-curves are only plotted at AM1.5 since they were very similar with the 10 % filter. Instead the IV-curves measured at AM1.5 one day later are plotted for comparison.

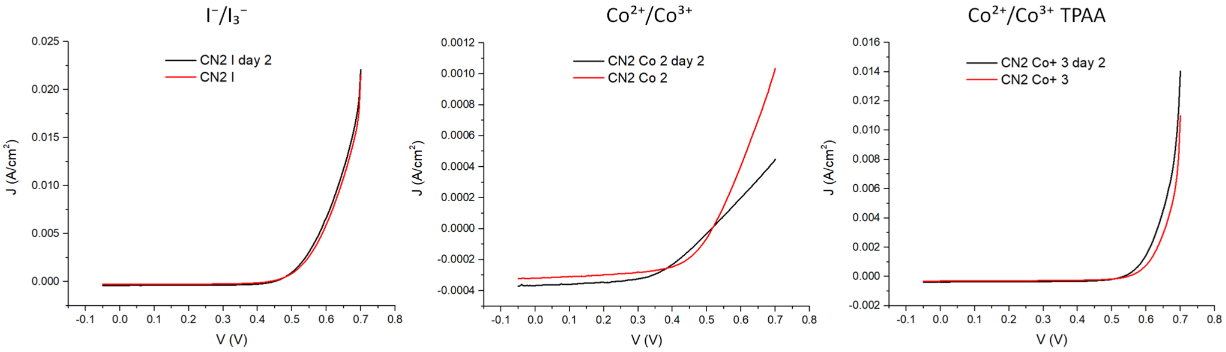

Figure 8.20: IV-curves from the selected best solar cells of each kind of FeCABCN2.

In Figure 8.21 the measured IPCE is plotted as a function of wavelength for the best selected solar cells of FeCABCN2 of each kind.

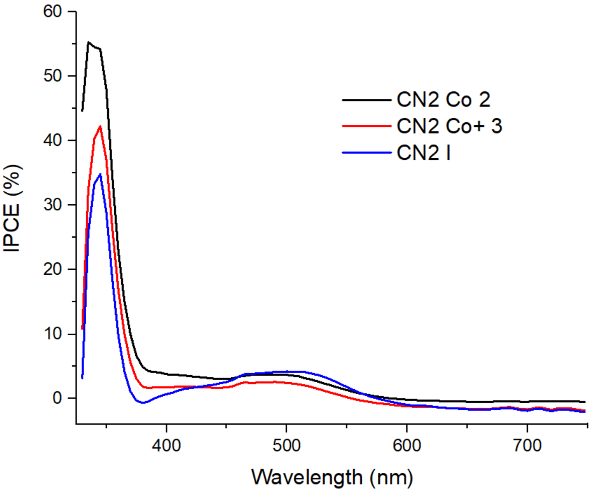

Figure 8.21: IPCE-curves from the selected best solar cells of each kind of FeCABCN2.

From the characterization it is seen that the best solar cell regarding the conversion efficiency is the "CN2 Co+ 3" that at best gave an efficiency of 0.133 %. This seems reasonable, since DSSCs fabricated with similar complexes in [41] gave an conversion efficiency of 0.13 % at best. The best solar cell regarding IPCE is the "CN2 I" with an IPCE of 3.83 % at 465 nm. However, FeCABCN2 gives working DSSCs for all three electrolytes with all solar cells having an efficiency around 0.1 % (except for the outlier cell "CN2 Co 3" which was probably not fabricated correctly), see Table 8.4. Focusing on the best solar cell of each kind, they all show characteristic IV-curves, Figure 8.20, and a contribution to the external quantum efficiency from FeCABCN2 in the IPCE-spectra (even if the titania peak is still higher), Figure 8.21. These measurements show that FeCABCN2 can serve as sensitizer in DSSCs since it injects electrons into the titania contributing to the photocurrent.

If one looks carefully in the graphs in Figures 8.19 and 8.21, the IPCE is sometimes below zero. This is not physically reasonable, but could not be corrected for in a simple way. The problem is thought to be associated with that the measurement setup is not optimized for measuring such low IPCE-values, so when comparing to the standard Si-solar cell the accuracy is not high enough and yields some negative values. This means that the IPCE of the solar cells in this thesis might be slightly higher than stated, but this is nothing that could be verified or corrected and does not change main conclusions in this thesis.

From the beginning, three functional DSSCs of each kind was desired but due to problems in the fabrication this could not be achieved. It would have been better to have three DSSCs of each kind fabricated in exactly the same way so an average of the characteristics could be formed. However, since the fabrication process is not optimized the results are not reflecting the full potential of the sensitizers. Therefore it is less important to be able to give the characteristics with higher statistical confidence.

Of the transparent cells, one of each kind (and a placebo with inert electrolyte) in Table 7.8 were successfully fabricated. The PIA-spectra of the cells in Table 7.8 can be seen in Figure 8.22.

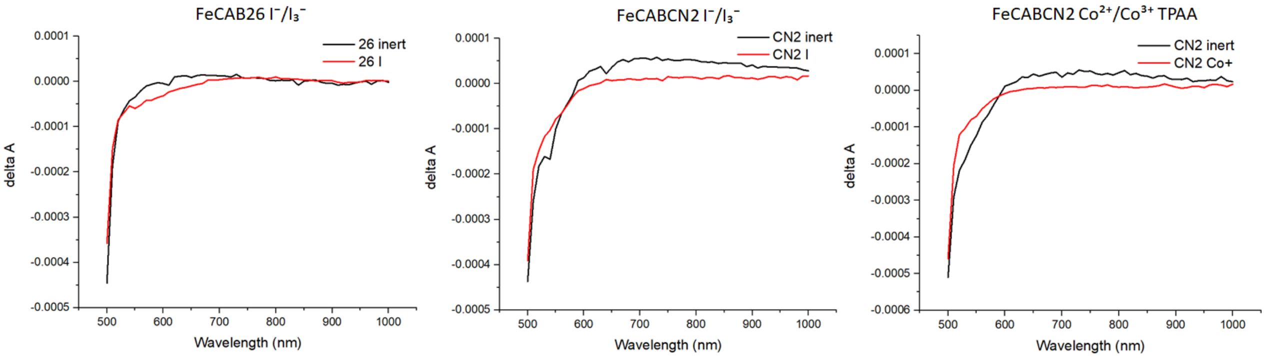

Figure 8.22: The difference in absorbance as a function of wavelength measured for the transparent cells of FeCAB26 and FeCABCN2.

The transparent DSSCs were fabricated to be able to perform PIA measurements that yield an indication of how the oxidized dye absorption spectra would look. In the PIA-spectra seen in Figure 8.22, the difference in absorbance is always higher for the inert electrolyte cell than the working electrolyte cell. This is due to the fact that the oxidized dye is not regenerated by the electrolyte for the inert cells upon excitation by the laser in the PIA measurement. Therefore, the wavelengths for which the inert and true electrolyte PIA spectra differs indicates where the oxidized dyes absorb. For FeCAB26 this is approximately from 520 nm to 700 nm and for FeCABCN2 this is approximately from 600 nm to 1000 nm.

8.5 DFT Calculations

To help understand all experimentally measured results through theory, a part of this thesis has consisted of running quantum chemistry calculations for the complexes FeCAB26, FeCABCN2 and to some extent for the ligand of FeCAB26. For each full complex an attempt was made to calculate all important electronic states (ground state, ^{3}MLCT, ^{3}MC and ^{5}MC) and their energies to be able to draw predicted Jablonski diagrams in Figure 8.26. For each full complex the ground state of the reduced and oxidized molecule was also calculated in order to approximate the redox levels in Figure 8.17. The Mulliken spin density on iron for FeCAB26 and FeCABCN2 in different electronic states together with the average Fe-ligand bond length and the energy of state are summarized in Table 8.5.

Table 8.5: For each electronic state of FeCAB26 and FeCABCN2 the Mulliken spin density on iron, the average iron-ligand bond length and the energy of the state are given.

Molecule	FeCAB26			FeCABCN2		
State	Spin den. Fe	Fe-Lig. bond (Å)	Energy (eV)	Spin den. Fe	Fe-Lig. bond (Å)	Energy (eV)
^{1}Fe(II)	0	1.96	0	0	1.96	0
^{3}Fe(II)	1.03	1.98	1.72	1.06	1.98	1.44
^{2}Fe(III)	0.99	1.98	5.45	0.99	1.98	5.03
^{2}Fe(I)	0.05	1.96	-3.20	0.08	1.97	-3.06
^{3}Fe(II)	2.09	2.09	1.32	2.10	2.08	1.24
^{5}Fe(II)	3.74	2.23	1.69	3.77	2.22	1.60

In Figures 8.23-8.25 the calculated spin densities of FeCAB26, FeCAB26 ligand and FeCABCN2 for the states given in Table 7.9 are shown. The states were calculated according to the procedure in section 7.8. The molecular structures in the pictures are optimized for the given electronic state.

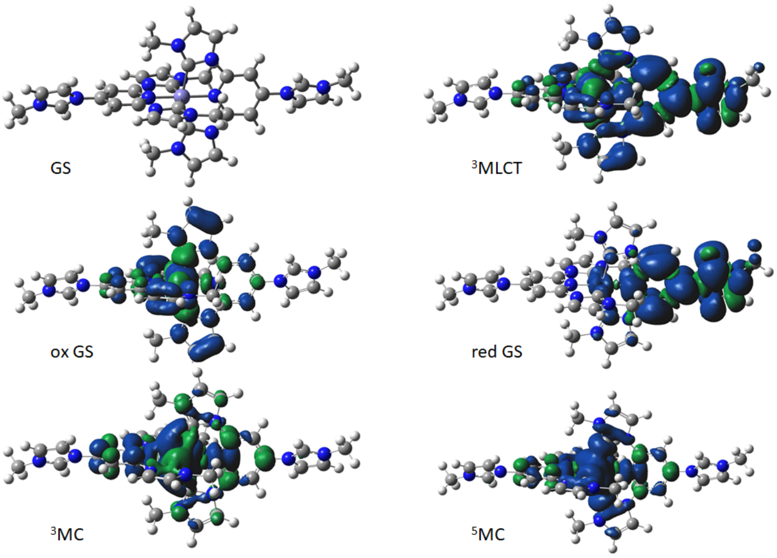

Figure 8.23: Calculated spin densities for the different optimized geometries of FeCAB26 with the assigned states in bottom left of each image.

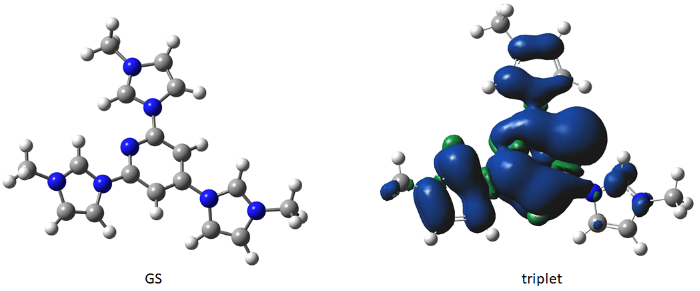

Figure 8.24: Calculated spin densities for the different optimized geometries of the ligand of FeCAB26 with the assigned states in bottom of each image.

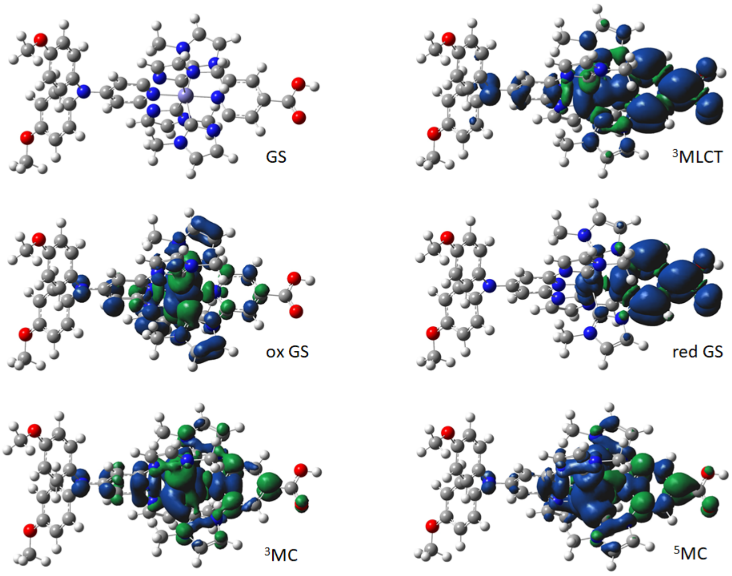

Figure 8.25: Calculated spin densities for the different optimized geometries of FeCABCN2 with the assigned states in bottom right of each image.

For all calculated states, where the geometry was optimized, a verification that it really was the intended state should be made. The verification can be done by looking at the spin density distribution (see Figures 8.23 to 8.25), the Mulliken spin density on iron and the average iron-ligand bond length (see Table 8.5). The ground state of each molecule should have the spin density zero everywhere since it is a singlet and all electrons are paired. The ground state Fe-ligand bond length can be used to compare with other bond lengths to find MC-states, since MC-state are further away along the reaction coordinate (see Figure 6.5, where ^{5}MC is furthest away and ^{3}MC between the ground state and the ^{5}MC-state). For an MC-state, a lot of unpaired electrons are centred at iron as can be seen in Figure 6.4 which means that a high Mulliken spin density is expected at iron for such a state (around two for ^{3}MC and four for ^{5}MC). In Table 8.5, four states fulfilling these requirements are found and indicated by MC, their spin density plots in Figures 8.23 and 8.25 also show a strong spin density on iron.

A ^{3}MLCT-state would instead have about the same Fe-ligand bond length as the ground state, as seen in Figure 6.5 b, and only one unpaired electron at iron since the other one is on the ligands, as seen in Figure 6.4. The two states fulfilling these requirements are indicated in Table 8.5 by MLCT and have a spin density on iron of about one and also a clear spin density on the ligands as seen in Figures 8.23 and 8.25. Also the oxidized and reduced complexes have about the same iron-ligand bond length, but the oxidized complexes have a spin density on iron of about one and the reduced complexes have a spin density on iron of about zero. This is explained by the fact that if a dye loses one electron and gets oxidized, the electron is removed from the t_{2g} metal-centred orbitals creating one unpaired electron on iron giving a spin density of one. If instead a dye gains one electron and gets reduced, the electron is put in a ligand-centred π^*-orbital and the spin on iron is unchanged. This is also seen in the Figures 8.23 and 8.25, the oxidized states have spin densities centred on iron and the reduced states have spin densities centred on the ligands.

In Figure 8.26, Jablonski diagrams for FeCAB26 and FeCABCN2 have been drawn according to the calculated energies from the optimized states in DFT.

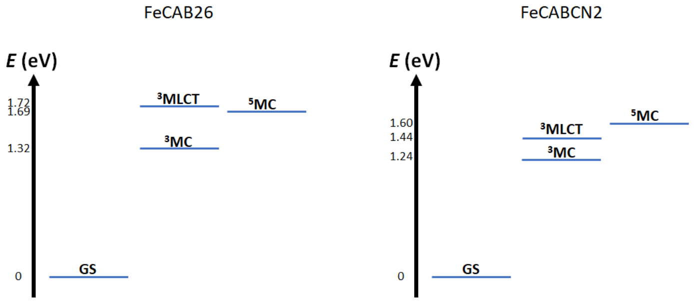

Figure 8.26: Jablonski diagram with selected electronic states of FeCAB26 (left) and FeCABCN2 (right). The energy levels were estimated from DFT calculations.

The Jablonski diagram of FeCAB26 is similar to the Jablonski diagram in Figure 6.5 a. The ^{5}MC-state is however higher in energy than the ^{3}MC-state. Both are not further than 0.4 eV from the ^{3}MLCT-state which indicates that the strategies outlined in section 6.3 have probably worked. In the Jablonski diagram of FeCABCN2, however, it is seen that the strategies have been even more efficient. Here the ^{5}MC-state is actually higher than the ^{3}MLCT-state, and the ^{3}MC-state is only 0.2 eV lower in energy than the ^{3}MLCT-state.

In Figures 8.27-8.29 important Kohn-Sham molecular orbitals of the complexes are shown. The orbitals were selected according to if they are involved in calculated singlet-singlet transitions from the ground state of the complexes, calculated by TD-DFT. Within the same figure, all orbitals have the same orientation. It is also indicated which orbital is HOMO and which is LUMO.

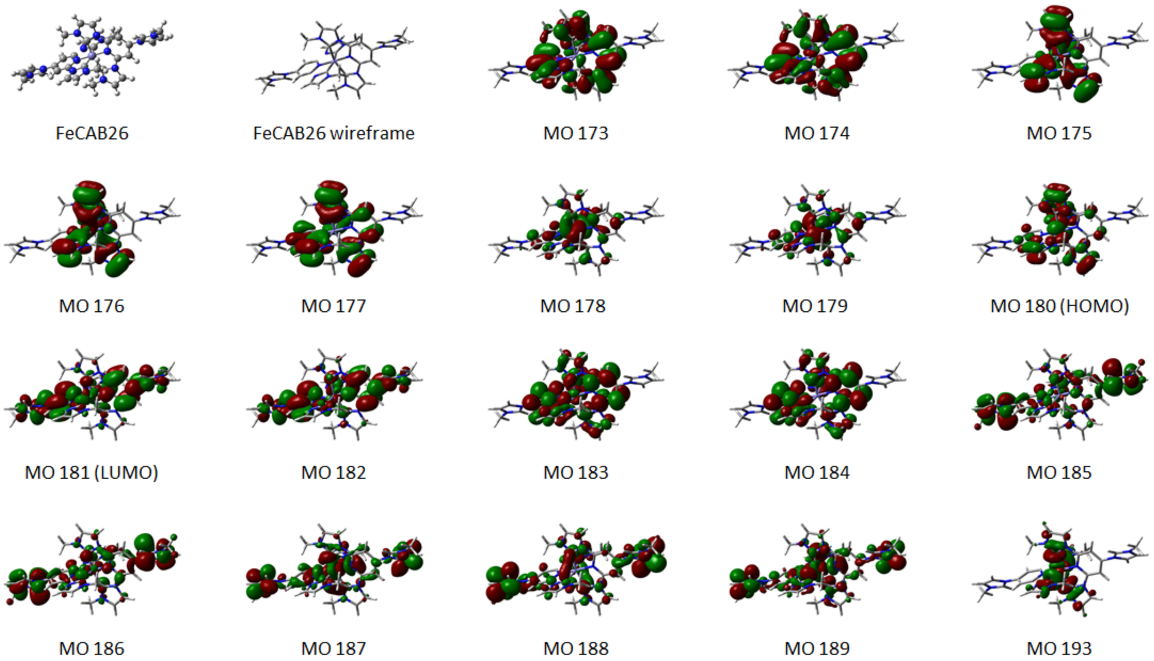

FeCAB26
FeCAB26 wireframe
MO 173
MO 174
MO 175
MO 176
MO 177
MO 178
MO 179
MO 180 (HOMO)
MO 181 (LUMO)
MO 182
MO 183
MO 184
MO 185
MO 186
MO 187
MO 188
MO 189
MO 193

Figure 8.27: Calculated Kohn-Sham molecular orbitals (MO), i.e. the electron densities for different electron orbitals of FeCAB26. The MOs are selected according to involvement in important transitions.

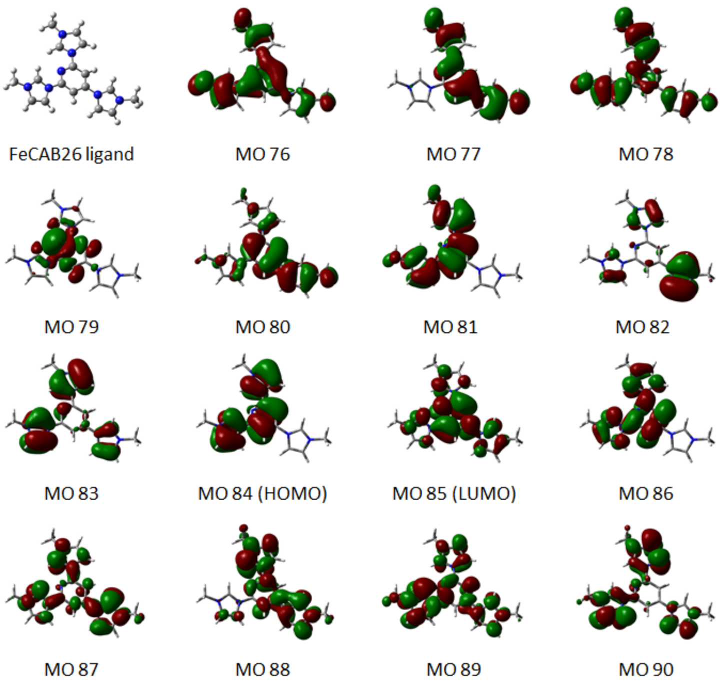

FeCAB26 ligand
MO 76
MO 77
MO 78
MO 79
MO 80
MO 81
MO 82
MO 83
MO 84 (HOMO)
MO 85 (LUMO)
MO 86
MO 87
MO 88
MO 89
MO 90

Figure 8.28: Calculated Kohn-Sham molecular orbitals (MO), i.e. the electron densities for different electron orbitals of the FeCAB26 ligand. The MOs are selected according to involvement in important transitions.

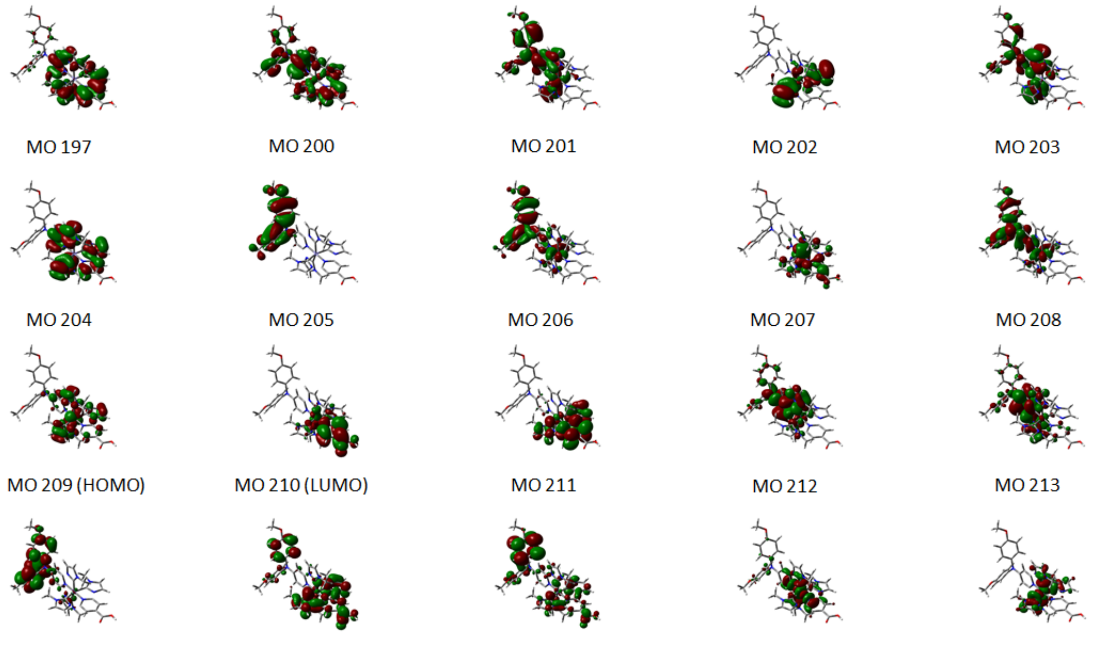

Figure 8.29: Calculated Kohn-Sham molecular orbitals (MO), i.e. the electron densities for different electron orbitals of FeCABCN2. The MOs are selected according to involvement in important transitions.

The calculated Kohn-Sham orbitals for FeCAB26 (Figure 8.27), the ligand of FeCAB26 (Figure 8.28) and FeCABCN2 (Figure 8.29), when studied carefully, show the mixing between the metal-centered orbitals and the ligand-centered orbitals as indicated in Figure 6.3 c. Some main features for the orbitals of full complexes FeCAB26 and FeCABCN2 are that:

- orbitals up to HOMO consist of mixtures between the metal-centered t_{2g}-orbitals and different ligand-centered π-orbitals, see for example MO 280 in Figure 8.27
- orbitals from LUMO and up consist of mixtures between metal-centered t_{2g}-orbitals and different ligand-centered π^*-orbitals, see for example MO 210 in Figure 8.29, or metal-centered e_g-orbitals and different ligand-centered σ^*-orbitals, see for example MO 218 in Figure 8.29
- some orbitals have very little contribution from the metal and are almost pure ligand-centered orbitals, see for example MO 177 in Figure 8.27 and MO 216 in Figure 8.29

For the ligand of FeCAB26, the situation is simpler. All orbitals up to HOMO are different π-orbitals and all orbtials from LUMO and up are different π^*-orbitals, of the orbitals included in Figure 8.28.

For all species, TD-DFT calculations were finally run to get material to simulate absorption spectra. The simulated absorption spectra were then compared to the experimentally measured absorption spectra to be able to understand the origin of spectral features. The 40 first singlet-singlet transitions of FeCAB26 are tabulated in Appendix Table 12.1, and a selection of the in this section discussed transitions are shown in Table 8.6. The transitions were calculated by TD-DFT on the ground state of FeCAB26 and yielded information about the transition energy/wavelength, the oscillator strength and the involved Kohn-Sham orbitals.

Table 8.6: Selected allowed transitions from the ground state of FeCAB26 (singlet to singlet), calculated with TD-DFT. For each transition, the most important Kohn-Sham molecular orbitals involved are stated.

Excited state	**Energy (eV)**	**Wavelength (nm)**	**Oscillator strength**	**Main molecular orbitals involved**
6	2.8138	440.63	0.2287	178->182, 179->181, 180->184
9	3.0536	406.03	0.2968	180->184, 179->181, 178->182
19	3.7788	328.1	0.0141	180->185
20	3.7913	327.02	0.0138	180->186
32	4.3136	287.42	0.1797	177->183

The data on oscillator strength and transition wavelength from Table 12.1 were used to simulate an absorption spectrum of FeCAB26. The simulated absorption spectrum is seen in Figure 8.30. Note that the calculations do not reach wavelengths shorter than 278 nm, therefore the spectral features beyond this point are not correct.

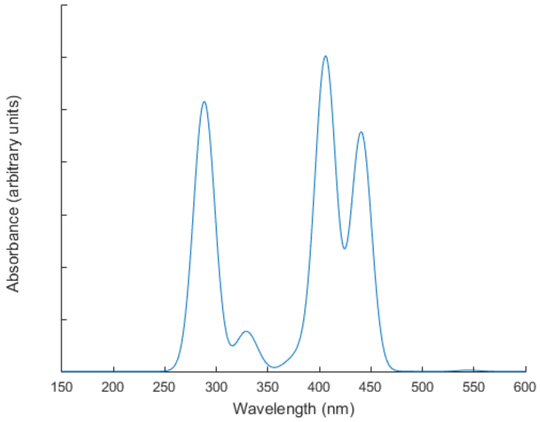

Figure 8.30: A simulated absorption spectrum of FeCAB26 from the transitions calculated in Table 12.1.

The first peak (longer wavelengths to shorter) in Figure 8.30 is around 440 nm and mainly come from the 6th transition in Table 8.6. This transition mainly involves excitations from orbitals 178, 179 and 180 to orbitals 182, 181 and 184. Orbitals 178-180 as seen in Figure 8.27 have large metal t_{2g} contribution and some ligand π contribution- Orbitals 181, 182, 184 as seen in Figure 8.27 have large ligand π^* contribution and some metal t_{2g} contribution for MOs 181-182. This means that the electron is excited from metal-centered orbitals to ligand-centered orbitals. Thus it is an excitation to an MLCT-state and the peak is probably the first MLCT-peak in the absorption spectrum of FeCAB26 (Figure 8.6 a) at 495 nm. TD-DFT calculations of excitations in MLCT-bands are not that accurate, and both the wavelength and the oscillator strength can be wrong. However, the qualitative information about what transitions there are and which main orbitals they involved are correct.

The next peak in Figure 8.30 at around 400 nm comes from mainly the 9th transition in Table 8.6 and it involvs exactly the same orbitals as for the 6th transition. Thus, also this peak is an MLCT-peak and it is assigned as the second peak in the absorption spectrum of FeCAB26 (Figure 8.6 a) at 411 nm. The third peak in Figure 8.30 at around 330 nm comes from mainly the 19th and 20th transitions in Table 8.6 consisting of excitations from MO 180 to MOs 185 and 186. MO 180 is the HOMO of the system and is an orbital of strong metal t_{2g} character with some ligand π contributions. MOs 185 and 186 have strong ligand π^* character with some metal t_{2g} contributions. Thus this peak is also a part of the MLCT absorption band since it involves MLCT transitions. The peak is not seen in the absorption spectrum of FeCAB26 (Figure 8.6 a) but is maybe not as strong as indicated by the calculations probably it gets covered by other signals/incorporated in other peaks.

The last calculated peak in Figure 8.30 at around 290 nm is mainly comprised of the 32nd transition in Table 12.1. The transition involves orbitals 177 only consisting of ligand π, and 183 mostly consisting of ligand π^*. This transition (together with some transitions around it if one investigates each transition carefully) is ligand-centered and not a part of the MLCT-band. The peak is also at almost the same wavelength as the first ligand absorption part of the FeCAB26 absorption spectrum, see Figure 8.6 a. Since the simulated peak is clearly ligand-centered, this helps prove that the 298 nm peak in the FeCAB26 absorption spectrum indeed is dominated by the ligand part of the molecule.

The 30 first singlet-singlet transitions of the ligand of FeCAB26 are tabulated in Appendix Table 12.2. The transitions were calculated by TD-DFT on the ground state of the ligand and yielded information about the transition energy/wavelength, the oscillator strength and the involved Kohn-Sham orbitals. The data on oscillator strength and transition wavelength in Table 12.2 were used to simulate an absorption spectrum of the ligand of FeCAB26. The simulated absorption spectrum is seen in Figure 8.31. Note that the calculations do not reach wavelengths shorter than 183 nm, therefore the spectral features beyond this point are not correct.

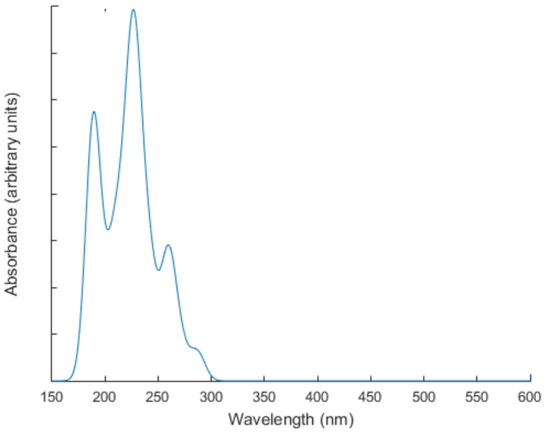

Figure 8.31: A simulated absorption spectrum of the ligand of FeCAB26 from the transitions calculated in Table 12.2.

The absorption spectrum of the FeCAB26 ligand was simulated, to be able to compare to the simulated absorption spectrum of the full complex FeCAB26, see Figure 8.30. TD-DFT calculations should be more accurate for the simpler ligand molecule than the full transition-metal complexes, and thus the wavelength scale should be almost correct. In the experimentally measured absorption spectrum of the ligand, see Figure 8.8 a, two peaks at 290 nm and 224 nm before the limit of the absorption spectrometer is reached. The simulated absorption spectrum, if cut at around 215 nm is absorbing in the same wavelength range but is a bit more resolved than the experimentally measured one (due to the choice of linewidth of the Gaussian functions in the simulation).

The 30 first singlet-singlet transitions of FeCABCN2 are tabulated in Appendix Table 12.3, and a selection of the in this section discussed transitions are shown in Table 8.7. The transitions were calculated by TD-DFT on the ground state of FeCABCN2 and yielded information about the transition energy/wavelength, the oscillator strength and the involved Kohn-Sham orbitals.

Table 8.7: Selected 30 allowed transitions from the ground state of FeCABCN2 (singlet to singlet), calculated with TD-DFT. For each transition, the most important Kohn-Sham molecular orbitals involved are stated.

Excited state	**Energy (eV)**	**Wavelength (nm)**	**Oscillator strength**	**Main molecular orbitals involved**
3	2.6191	473.38	0.2115	207->210, 209->211
8	3.1265	396.56	0.0157	207->218, 208->211
9	3.1351	395.47	0.3202	209->211, 208->212
10	3.1901	388.65	0.0692	209->213, 209->211
11	3.2233	384.65	0.0101	207->211
17	3.5191	352.32	0.1299	208->212, 209->223
24	3.8542	321.69	0.0368	206->212, 206->213
25	3.9084	317.22	0.0109	200->210, 201->210, 209->215
26	3.9238	315.98	0.0004	201->210, 200->210
27	3.965	312.7	0.0391	209->215, 209->216
28	4.0713	304.53	0.0002	208->215, 208->216
29	4.1044	302.08	0.0035	208->223, 197->210, 206->223
30	4.1588	298.13	0.0477	208->214

The data on oscillator strength and transition wavelength in Table 12.3 were used to simulate an absorption spectrum of FeCABCN2. The simulated absorption spectrum is seen in Figure 8.32. Note that the calculations do not reach wavelengths shorter than 298 nm, therefore the spectral features beyond this point are not correct.

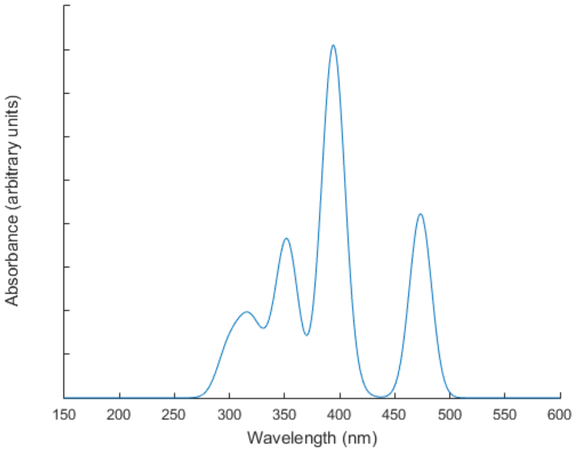

Figure 8.32: A simulated absorption spectrum of FeCABCN2 from the transitions calculated in Table 12.3.

The first peak (longer wavelengths to shorter) in Figure 8.32 is around 470 nm and mainly come from the 3rd transition in Table 8.7. This transition mainly involves excitations from orbitals 207 and 208 to orbital 210. Orbitals 207 and 208 has, as seen in Figure 8.29 big contributions of metal-centered t_{2g}-orbitals and contributions also from π-orbitals on the different ligands. MO 210 is the LUMO of FeCABCN2 and contains big contributions of π^* on the ligand with the carboxylic group and also some metal t_{2g} contributions. This transition is thus an excitation to an MLCT-state, and probably corresponds to the first peak in the FeCABCN2 absorption spectrum at 468 nm, see Figure 8.10 a. The involved orbitals suggest a transition of an electron from iron to the ligand with the carboxylic group, which is just how the molecule is supposed to behave according to the design. The push-pull functionality seems to be working at least in the first absorption peak.

The second peak in Figure 8.32 at around 390 nm has contributions at least from transitions 8-11 in Table 8.7, but the strongest contribution come from the 9th transition. This transition mainly involve excitations from orbitals 209 to 211 and 208 to 212. From MO 209 to MO 211 the electron moves from a rather metal-centred t_{2g}-orbital to a more ligand centred π^*-orbital on the ligand of the carboxylic group. From MO 208 to MO 212 the electron moves from a rather metal-centred t_{2g}-orbital to a more ligand centred π^*-orbital on the other ligand. Thus this is also an MLCT-peak, however the push-pull effect is not as prominent as for the first MLCT-peak. The peak is probably corresponding to the peak at 395 nm in the FeCABCN2 absorption spectrum (Figure 8.10 a) even though it is higher in absorbance than the first peak.

The third peak in Figure 8.32 at around 350 nm mainly consist of transitions 17th in Table 8.7, involving transitions MO 208 to MO 212 and MO 209 to MO 223. The excitation from MO 208 to 212 is from an orbital with metal t_{2g} character and some ligand π character to an orbital metal t_{2g} character and some ligand π^* character. The excitation from MO 209 to 223 is from an orbital of strong metal t_{2g} character to an orbital of metal e_g character and with some ligand σ^* character. The transition is thus rather metal-centred and is probably not part of the MLCT-band. The position of the peak is right between the MLCT-band and the probably ligand part of the FeCABCN2 absorption spectrum, Figure 8.10 a. Metal-centred transitions are in reality very weak, and the transition oscillator strength has probably been exaggerated by the calculation. In the measured absorption spectrum the peak can not be distinguished probably due to it being covered by the other peaks.

The last broad peak in the simulated absorption spectrum (Figure 8.32) at around 315 nm contain contributions from transitions 24-30 in Table 8.7. When closely investigated, many of the involved orbitals have their main electron density on the ligands, and the excitations are mainly from π- to π^*-orbitals. This means that this is the start of the absorption spectrum consisting of ligand-centred transitions. More calculated transitions would have been needed to see the true features of this part of the spectrum, probably peaks of higher oscillator strength will come and cover this peak. Hovewer, the TD-DFT calculation gives a hint that the peaks not yet assigned in the FeCABCN2 absorption spectrum (Figure 8.10 a), that is the peaks thought to coming from ligand absorption, indeed probably come from ligand absorption.

9 Discussion

In this section a discussion of how the characterized properties relate to the solar cell device performance will be led, in agreement with the goal of this thesis. The limitations of each molecule for usage as a sensitizer in DSSCs, will be assessed. The discussion is based on the, for DSSCs, important processes indicated by numbers in Figure 9.1.

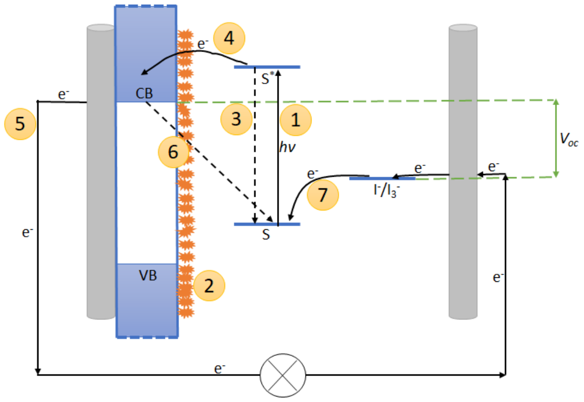

Figure 9.1: The dye sensitized solar cell working scheme. CB/VB are the conduction/valence band of the semiconductor. S (S*) is the (excited) sensitizer/dye. I^- /I_3^- is the regeneration redox couple. The silver coloured rods are the electrodes and the orange particles are the dye molecules (not to scale).

The indicated processes in Figure 9.1 are:

1. light absorption of the dye molecule
2. dye loading of sensitizer on titania
3. relaxation of excited state to ground state
4. injection of electrons into titania
5. extraction of current from the DSSC
6. recombination back to the ground state
7. regeneration of oxidized dye by electrolyte

The sensitizer in a DSSC should ideally absorb a lot of light over the whole visible light range, and how well it absorbs is reflected by the extinction coefficient. To be able to understand the features in the extinction coefficients for FeCAB26 and FeCABCN2 (Figures 8.1 and 8.3), TD-DFT calculations were used to simulate the shape of the spectra and explain them. Also, the extinction coefficient of the ligand of FeCAB26 was measured (Figure 8.2) and simulated (also, only the shape) to be able to distinguish if a part of the absorption arises almost entirely from the ligands. The results show that indeed the extinction coefficients of FeCAB26 and FeCABCN2 contain two main features: a charge-transfer band and a ligand-centred absorption band. For DSSC applications, the charge-transfer band make up the important absorption. This is because the electron upon excitation should move from the metal to the ligand attached to the titania surface. The excitations making up the charge-transfer band was shown in the DFT calculations to take the electron from metal-centred orbitals to ligand-centred orbitals, as desired. This means that light impinging on the DSSCs of wavelength approximately 400-500 nm will be absorbed by the sensitizer in the solar cell and contribute to the device performance.

It is not enough for a solar cell to have absorption in the visible range, the absorbance must also be sufficiently high when attached to the titania. This depends on two things; again, the extinction coefficient and also the dye loading. The measured extinction coefficients of the molecules are not considered low comparing to other similar complexes, but are lower than the best performing DSSC dyes (see for example [37]). Since the extinction coefficient is a fundamental property reflecting how much the molecules absorb, it will affect the performance, but in this case it is probably not the limiting factor for the device performance. The dye loading, meaning how densely molecules are attached to the titania surface, will affect how well the fabricated solar cells will absorb. The dye loading is affected by the anchoring group on the molecule, and in this thesis two different anchoring groups are used. Since the films sensitized with FeCAB26 looked paler than the ones sensitized with FeCABCN2, it was concluded that the more conventional carboxylic anchoring group gave the highest dye loading. This was also reflected in the device performance of the solar cells. Even if both molecules were able to sensitize films of titania, probably the dye loading is one of the major limitations for FeCAB26 as a sensitizer in DSSCs.

It is clear from the TD-DFT calculations that both complexes form a charge transfer when excited in the appropriate band, because the electron density moves from metal-centred orbitals to ligand-centred orbitals. However, a main difference between the two complexes is that FeCAB26 is homoleptic whereas FeCABCN2 is heteroleptic. Being homoleptic means there is no preference for an excited electron to go to one ligand more than the other. This means that the electron might not go to the ligand bound to the TiO_2 and become injected.[25] Even if it is shown from TA measurements that some of the electrons get injected, being homoleptic is one of the major drawbacks for FeCAB26 as a sensitizer in DSSCs. Contrary to FeCAB26, FeCABCN2 is a heteroleptic molecule designed to be a sensitizer in DSSCs. The ligand with the carboxylic anchoring group is designed to pull away the electron from iron towards the titania attached to it, upon excitation to MLCT-states. Exactly this effect was seen in the calculated molecular orbitals involved in the transition assigned to the strongest peak in charge-transfer band of FeCABCN2. Therefore, the design strategy seems to work theoretically, and also the TA data of FeCABCN2 sensitized on titania shows injection. The difference in molecular design between FeCAB26 and FeCABCN2 is also reflected in the device performance, since FeCABCN2 is generating a photocurrent in the DSSCs whereas FeCAB26 is probably not.

After the dye has been excited to the MLCT-states in the DSSC, three different processes within the scope of this thesis can occur:

- The excited electron can be injected into the titania and from there be extracted as current, this is the desired process.
- The excited electron can be injected into the titania and then recombine with the hole, and thus go back to the molecule which returns to its ground state.
- The excited electron can through non-radiative relaxation return the molecule to its ground state, and thus never be injected into the titania.

Recombination and relaxation are thus two processes that one wants to avoid in DSSCs.

Relaxation is probably a major drawback for both complexes in this thesis, since the lifetimes of the ^{3}MLCT-states (35.8 ps and 20.8 ps, measured with TAS, see Figures 8.13 and 8.15) are relatively short. When the molecules are excited in the charge-transfer band, an electron is excited to the ^{1}MLCT-state. From there an ultrafast intersystem crossing occurs and it ends up in the ^{3}MLCT-state within less than 1 ps. It is from this state that the electron should be injected into the conduction band of titania, therefore the lifetime of this state is measured and the emission from this state was probed. The short lifetimes, consistent with the fact that no emission was observed from these states, indicate that for both complexes there is an efficient relaxation pathway. As seen in Figure 6.5 b, the pathway goes via the MC-states to the ground state.

To try to make the relaxation pathway less efficient, and thus prolong the lifetime of the ^{3}MLCT-state, most of the strategies stated in section 6.3 are incorporated in the design of the molecules. The strategies should result in a stabilization of the ^{3}MLCT-state and a destabilization of the MC-states. In the Jablonski diagrams obtained from DFT calculations, Figure 8.26, the outcome of the design efforts can be seen. The diagrams show that the initially bad positions of the excited states for Fe-complexes, Figure 6.5 a, were improved. For FeCABCN2, the ^{5}MC-state is even shifted to energies higher than the ^{3}MLCT-state. The position of the ^{5}MC-states in the Jablonski diagrams in Figure 8.26 shows that the relaxation pathway only goes via the ^{3}MC-states for the complexes. Even if both complexes show injection (from TA measurements), relaxation is a major drawback for both complexes and maybe the factor limiting the device performance of FeCABCN2. To be able to investigate this, a suggestion for further characterization beyond the scope of this thesis would be to quantify the efficiency of the injection.

The electrons that are actually injected into the TiO_2, suffer from the other parasitic process; recombination. From TA measurements, the lifetime of the recombination for the complexes was determined to be on the order of ns (see Figures 8.13 and 8.15). This means that the oxidized dyes are rather long-lived compared to the ^{3}MLCT-states, but not within the scope of electrolyte regeneration times. The electrolyte dye-regeneration is considered to happen on the ms-timescale since it is diffusion driven, which is a problem. To mitigate the recombination, one can thus either prolong the lifetime of the oxidized dye or improve the electrolyte regeneration time. FeCABCN2 is designed as a push-pull complex, meaning that the ligand attached to titania is supposed to pull away the electron from iron and the other ligand is designed to pull away the hole from iron (thus pushing away the electron). This design helps to mitigate recombination since the molecule contains a built-in electric field keeping the separated electron and hole away from each other.[3] As FeCAB26 is homoleptic, there is no internal electric field within the molecule trying to keep the electron and hole separated.[25] Again, the difference in molecular design is reflected in the device performance of the fabricated DSSCs.

To investigate if recombination was the limiting factor of the DSSC device performance, the IV-characteristics were measured with a 10 % filter and PIA-measurements were performed. If the IV-characteristics were better with the 10 % filter, this would be an indication of too short lifetime of the electron and thus potentially also of the oxidized dye. No significant improvements were however seen for the DSSCs and from the PIA measurements it is seen that the oxidized dyes are regenerated by some of the electrolytes. Also, the electrolyte that was supposed to have the shortest regeneration time did not yield significantly better solar cells. Therefore, the recombination was probably not the limiting factor for any of the DSSCs (although it still contributed in making the device performance worse).

Choosing an appropriate electrolyte is not only about picking the one of shortest dye regeneration time. The most important property of the electrolyte is the redox potential, and the redox potential of the electrolytes used in this thesis are indicated in Figure 8.17. The further away from the conduction band edge of titania the redox potential is, the higher the open circuit voltage will be (which is good regarding device performance). But there still needs to be a difference in energy between the redox potential of the electrolyte and the dye to have a thermodynamic driving force to regenerate the oxidized dye. If the difference is smaller, the regeneration will take longer time. In Figure 8.17, it is seen that the difference between the redox potential of FeCABCN2 and TPAA/TPAA$^+$ is very small, which could be the reason why the Co^{2+}/Co^{3+} electrolyte did not give better results with the TPAA additive than without it. FeCABCN2 probably has a higher redox potential than the dyes used in [36], and therefore the electrolyte might not be working as expected for our molecule.

The stability of a sensitizer is also important, since the solar cells should work for some years to be able to commercialize. For FeCAB26, stability was not a problem, but for FeCABCN2 the absorption spectrum changed with time which is an indication of a stability issue (see Figure 8.5). However, the absorption spectrum also changed with concentration, and the effect was assigned as agglomeration effects. To see that agglomeration effects are not affecting the absorption of the solar cells, the absorption of a titania film with high dye loading can be studied. It is however non-trivial to measure the absorption of such a film (the transparent half-cells prepared for TA measurements do not have sufficient dye loading and the real solar cells have a scattering layer making them non-transparent). Therefore, these measurements were beyond the scope of this thesis, but are a suggestion for further characterization.

As for all other new dyes, DSSCs with FeCAB26 and FeCABCN2 as sensitizers would have needed an optimized fabrication process to reach their full potentials as sensitizers in solar cells. At this stage, there are many unoptimized parameters impacting the device performances and it is not possible to judge for each molecule which problem is limiting the device performance the most. Nevertheless, indications of what are probably the greatest limitations of each molecule have been given throughout the discussion. Samples of both molecules were left in Uppsala, for eventual further optimization of the fabrication procedure beyond the scope of this thesis. The information yielded from characterization of the optimized solar cells would be the important next step to continue improving the Fe-complexes designed as sensitizers in DSSCs.

10 Conclusions

In this thesis, the two Fe-complexes FeCAB26 and FeCABCN2 were characterized and evaluated for potential usage as sensitizers in DSSCs. Since the molecules were different (homoleptic vs heteroleptic, different anchoring groups, different ligands) slightly different approaches were taken upon characterization. For homoleptic FeCAB26 also the ligand was partly characterized to learn how ligands influence the molecular properties. For heteroleptic FeCABCN2 the stability was investigated since the absorption spectrum changed with concentration and time. Even though the anchoring groups were different, both molecules were able to sensitize films both of TiO_2 and Al_2O_3. Even if the ligands had different side-groups on the pyridine rings, what they had in common was that they were all N-heterocyclic carbenes. Therefore, a lot of qualitative analysis apply to both of the molecules.

The extinction coefficient is important since it states for which wavelengths the molecule absorbs and how strongly, which is the first requirement to become a sensitizer in DSSCs. Both complexes exhibit MLCT-absorption in the visible range (whose nature was confirmed by TD-DFT calculations) at an extinction coefficient in the same order of magnitude as similar complexes. The FeCABCN2 extinction coefficient is the highest, thus this complex shows the greatest potential. However, it seems like the absorption spectrum of FeCABCN2 is not completely stable in solution. This is tentatively assigned to agglomeration and can be avoided by working at low concentrations and sonicating the sample.

Neither FeCAB26 or FeCABCN2 showed emission from the MLCT-states, but probably weak emission (not detectable by eye) from the respective ligands. This stands in agreement with the fitted lifetimes from TA spectroscopy where the lifetime of these molecules in solution is within 15-17 ps. However, injection in DSSCs can be ultrafast and the results from TA spectroscopy show injection for both complexes when sensitized on TiO_2. FeCABCN2 yielded solar cells that did work and had a contribution in the external quantum efficiency from the sensitizer. Even if the solar cells operated at low efficiencies, a proof of concept that FeCABCN2 could work as a sensitizer in DSSCs was shown. As expected, FeCABCN2 sensitized solar cells were better than FeAB26 sensitized ones probably due to the fact that the molecule has a better anchoring group and a push-pull functionality.

Fabrication of DSSCs was a complicated process full of parameters to optimize, and to be able to say more specifically what were the major drawbacks with the molecules one would need to spend several months optimizing the fabrication process first. This might be done in the future, together with more characterization of the molecular properties. The optical characterization done for both molecules will however be useful also beyond the scope of solar cells. But most importantly, this thesis has been a step in the process of finding better iron-based sensitizers for DSSCs that might one day lead to a commercially available solar cell.

11 References

[1] S. FN-förbundet, “Fn-förbundet una sweden,” 2018. https://fn.se/, Accessed: 2019-01-09.

[2] M. Abrahamsson, “Solar energy conversion using iron polypyridyl type photosensitizers – a viable route for the future?,” vol. 44, pp. 285–295, 2017.

[3] C. S. Ponseca, P. Chábera, J. Uhlig, P. Persson, and V. Sundström, “Ultrafast Electron Dynamics in Solar Energy Conversion,” *Chemical Reviews*, vol. 117, pp. 10940–11024, aug 2017.

[4] B. S. Honsberg, Christiana, “Pveducation,” 2019. https://www.pveducation.org/, Accessed: 2019-01-08.

[5] Nationalencyklopedin, “Nationalencyklopedin, fotosyntes,” 2018. http://www.ne.se/uppslagsverk/encyklopedi/lång/fotosyntes, Accessed: 2018-08-20.

[6] M. O’Regan, Brian, Grätzel, “A low-cost, high-efficiency solar cell based on dye-sensitized colloidal TiO2 films,” *Letters To Nature*, vol. 353, pp. 737–740, 1991.

[7] T. C. B. Harlang, Y. Liu, O. Gordivska, L. A. Fredin, C. S. Ponseca, P. Huang, P. Chábera, K. S. Kjaer, H. Mateos, J. Uhlig, R. Lomoth, R. Wallenberg, S. Styring, P. Persson, V. Sundström, and K. Wärnmark, “Iron sensitizer converts light to electrons with 92% yield,” *Nature Chemistry*, vol. 7, pp. 883–889, nov 2015.

[8] P. Chábera, K. S. Kjaer, O. Prakash, A. Honarfar, Y. Liu, L. A. Fredin, T. C. B. Harlang, S. Lidin, J. Uhlig, V. Sundström, R. Lomoth, P. Persson, and K. Wärnmark, “Fe II Hexa N -Heterocyclic Carbene Complex with a 528 ps Metal-to-Ligand Charge-Transfer Excited-State Lifetime,” *The Journal of Physical Chemistry Letters*, vol. 9, pp. 459–463, feb 2018.

[9] P. Chábera, Y. Liu, O. Prakash, E. Thyrhaug, A. E. Nahhas, A. Honarfar, S. Essén, L. A. Fredin, T. C. B. Harlang, K. S. Kjær, K. Handrup, F. Ericson, H. Tatsuno, K. Morgan, J. Schnadt, L. Häggström, T. Ericsson, A. Sobkowiak, S. Lidin, P. Huang, S. Styring, J. Uhlig, J. Bendix, R. Lomoth, V. Sundström, P. Persson, and K. Wärnmark, “A low-spin Fe(iii) complex with 100-ps ligand-to-metal charge transfer photoluminescence,” *Nature*, vol. 543, pp. 695–699, mar 2017.

[10] A. Hagfeldt and M. Grätzel, “Molecular Photovoltaics,” *Accounts of Chemical Research*, vol. 33, pp. 269–277, may 2000.

[11] J. L. Atkins, P., *Chemical Principles - the Quest for Insight, 5th edition.* W. H. Freeman, 5 ed., 2010.

[12] A. G. Sharpe, *Inorganic Chemistry, 2nd Edition.* Longman Scientific and Technical, 2 ed., 1986.

[13] Y. Liu, P. Persson, V. Sundström, and K. Wärnmark, “Fe N -Heterocyclic Carbene Complexes as Promising Photosensitizers,” *Accounts of Chemical Research*, vol. 49, pp. 1477–1485, aug 2016.

[14] S. Svanberg, *Atomic and Molecular Spectroscopy, Basic Aspects and Practical Applications, 4th Edition.* Springer, 4 ed., 2004.

[15] J. Chen and W. R. Browne, “Photochemistry of iron complexes,” *Coordination Chemistry Reviews*, vol. 374, pp. 15–35, nov 2018.

[16] T. M. C. Saleh, B. E. A., *Fundamentals of Photonics, 2nd Edition.* Wiley, 2 ed., 2007.

[17] A. Juris, V. Balzani, F. Barigelletti, S. Campagna, P. Belser, and A. von Zelewsky, “Ru(II) polypyridine complexes: photophysics, photochemistry, eletrochemistry, and chemiluminescence,” *Coordination Chemistry Reviews*, vol. 84, pp. 85–277, mar 1988.

[18] J. Klán, P., Wirz, *Photochemistry of Organic Compounds - From Concepts to Practice.* Wiley, 1 ed., 2009.

[19] L. A. Fredin, M. Pápai, E. Rozsályi, G. Vankó, K. Wärnmark, V. Sundström, and P. Persson, “Exceptional Excited-State Lifetime of an Iron(II)– N -Heterocyclic Carbene Complex Explained,” *The Journal of Physical Chemistry Letters*, vol. 5, pp. 2066–2071, jun 2014.

[20] J. K. McCusker, "Femtosecond Absorption Spectroscopy of Transition Metal Charge-Transfer Complexes," *Accounts of Chemical Research*, vol. 36, pp. 876–887, dec 2003.

[21] O. S. Wenger, "Photoactive Complexes with Earth-Abundant Metals," *Journal of the American Chemical Society*, vol. 140, pp. 13522–13533, oct 2018.

[22] A. Mc Naught and A. Wilkinson, *IUPAC Compendium of Chemical Terminology, Gold Book, ver. 2.3.3.* Research Triagle Park, NC: IUPAC, 1997.

[23] M. N. Hopkinson, C. Richter, M. Schedler, and F. Glorius, "An overview of N-heterocyclic carbenes," *Nature*, vol. 510, pp. 485–496, jun 2014.

[24] M. Abrahamsson, M. Jäger, R. J. Kumar, T. Österman, P. Persson, H.-c. Becker, O. Johansson, and L. Hammarström, "Bistridentate Ruthenium(II)polypyridyl-Type Complexes with Microsecond 3 MLCT State Lifetimes: Sensitizers for Rod-Like Molecular Arrays," *Journal of the American Chemical Society*, vol. 130, pp. 15533–15542, nov 2008.

[25] A. A. Ünal, *Solar Energy Conversion.* Energy and Environment Series, The Royal Society of Chemistry, 2013.

[26] A. K. C. Mengel, C. Förster, A. Breivogel, K. Mack, J. R. Ochsmann, F. Laquai, V. Ksenofontov, and K. Heinze, "A Heteroleptic Push-Pull Substituted Iron(II) Bis(tridentate) Complex with Low-Energy Charge-Transfer States," *Chemistry - A European Journal*, vol. 21, pp. 704–714, jan 2015.

[27] F. N. Castellano, "Making iron glow," *Nature*, vol. 543, pp. 627–628, mar 2017.

[28] PerkinElmer, *LAMBDA UV/Vis and UV/Vis/NIR Spectrophotometers 850/950/1050*, 2007. https://www.perkinelmer.com/lab-solutions/resources/docs/BRO_LAMBDA8509501050.pdf.

[29] J. Clark, "Chemguide," 2004. https://www.chemguide.co.uk/index.html#top, Accessed: 2018-12-19.

[30] Horiba, *Fluorolog-3 with FluorEssence Operation Manual rev. G (2014-05-02).*

[31] R. Berera, R. van Grondelle, and J. T. M. Kennis, "Ultrafast transient absorption spectroscopy: principles and application to photosynthetic systems," *Photosynthesis Research*, vol. 101, pp. 105–118, sep 2009.

[32] H. Liu, Y. Bai, Y. Zhang, S. Ye, W. Xu, and Y. Zhou, "Graphical analysis of transient absorption spectra using the phasor approach," *Journal of the Optical Society of America B*, vol. 32, p. 1693, aug 2015.

[33] I. H. van Stokkum, D. S. Larsen, and R. van Grondelle, "Global and target analysis of time-resolved spectra," *Biochimica et Biophysica Acta (BBA) - Bioenergetics*, vol. 1657, pp. 82–104, jul 2004.

[34] T. Dittrich, *Materials Concepts for Solar Cells, 2nd edition.* World Scientific, 2 ed., 2018.

[35] U. D. of Energy, "National renewable energy laboratory," 2019. https://www.nrel.gov/pv/, Accessed: 2019-01-03.

[36] Y. Hao, W. Yang, L. Zhang, R. Jiang, E. Mijangos, Y. Saygili, L. Hammarström, A. Hagfeldt, and G. Boschloo, "A small electron donor in cobalt complex electrolyte significantly improves efficiency in dye-sensitized solar cells," *Nature Communications*, vol. 7, p. 13934, dec 2016.

[37] G. Boschloo and A. Hagfeldt, "Photoinduced absorption spectroscopy of dye-sensitized nanostructured TiO2," *Chemical Physics Letters*, vol. 370, pp. 381–386, mar 2003.

[38] H. M. C. Koch, Wolfram, *A Chemist's Guide to Density Functional Theory, 2nd edition.* Wiley-VCH, 2 ed., 2000.

[39] L. E. Roy, E. Jakubikova, M. G. Guthrie, and E. R. Batista, "Calculation of One-Electron Redox Potentials Revisited. Is It Possible to Calculate Accurate Potentials with Density Functional Methods?," *The Journal of Physical Chemistry A*, vol. 113, pp. 6745–6750, jun 2009.

[40] A. Vogler, "Phosphorescent iron complexes? Intraligand luminescence of solid Fe(II)(binap)Cl2 at room temperature," *Inorganic Chemistry Communications*, vol. 67, pp. 32–34, may 2016.

[41] T. Duchanois, L. Liu, M. Pastore, A. Monari, C. Cebrián, Y. Trolez, M. Darari, K. Magra, A. Francés-Monerris, E. Domenichini, M. Beley, X. Assfeld, S. Haacke, and P. Gros, "NHC-Based Iron Sensitizers for DSSCs," *Inorganics*, vol. 6, no. 2, p. 63, 2018.

12 Appendix

Table 12.1: The first 40 allowed transitions from the ground state of FeCAB26 (singlet to singlet), calculated with TD-DFT. For each transition, the most important Kohn-Sham molecular orbitals involved are stated.

Excited state	**Energy (eV)**	**Wavelength (nm)**	**Oscillator strength**	**Main molecular orbitals involved**
1	2.2739	545.25	0.0005	180->181
2	2.2763	544.67	0.0007	180->182
3	2.5739	481.69	0.0001	178->182, 179->181
4	2.6121	474.65	0	178->181, 179->182
5	2.8	442.79	0	180->183, 178->181, 179->182
6	2.8138	440.63	0.2287	178->182, 179->181, 180->184
7	3.0075	412.25	0.0013	179->187, 179->183, 179->189
8	3.0432	407.42	0.0007	178->187, 178->189, 178->183
9	3.0536	406.03	0.2968	180->184, 179->181, 178->182
10	3.1822	389.62	0.0077	178->183
11	3.2109	386.13	0.0075	179->183, 179->187, 179->189
12	3.3219	373.23	0.0043	179->184
13	3.3267	372.69	0.004	178->184
14	3.4122	363.35	0	180->183, 179->182, 178->181
15	3.5535	348.91	0.0001	180->187, 180->189
16	3.5703	347.27	0	180->193
17	3.6995	335.14	0.0052	177->181
18	3.706	334.55	0.0054	177->182
19	3.7788	328.1	0.0141	180->185
20	3.7913	327.02	0.0138	180->186
21	3.8193	324.62	0.0019	175->181, 176->182
22	3.8618	321.06	0	176->182, 175->181
23	3.8644	320.84	0	176->181, 175->182
24	3.8824	319.35	0	175->182, 176->181
25	4.1455	299.08	0.0003	178->185
26	4.1519	298.62	0.0046	179->186
27	4.1524	298.59	0.0001	179->185
28	4.1741	297.03	0	178->186
29	4.2531	291.51	0.0261	179->193, 174->181
30	4.2591	291.51	0.0261	174->182, 178->193
31	4.3087	287.76	0.0105	174->181, 179->193, 176->183
32	4.3136	287.42	0.1797	177->183
33	4.3163	287.25	0.0102	174->182, 178->193
34	4.38	283.07	0	177->184
35	4.3874	282.59	0.0011	176->183
36	4.3904	282.4	0.0012	175->183
37	4.4435	279.03	0.0007	173->181, 176->184
38	4.4482	278.73	0.0003	175->184, 173->182
39	4.4532	278.41	0.0028	176->184, 173->181, 180->188
40	4.4577	278.13	0.0031	173->182, 175->184

Table 12.2: The first 30 allowed transitions from the ground state of the ligand of FeCAB26 (singlet to singlet), calculated with TD-DFT. For each transition, the most important Kohn-Sham molecular orbitals involved are stated.

Excited state	**Energy (eV)**	**Wavelength (nm)**	**Oscillator strength**	**Main molecular orbitals involved**
1	4.3145	287.37	0.0574	84->85
2	4.4286	279.96	0.0002	83->85
3	4.4907	276.09	0.0249	82->85
4	4.6313	267.71	0.0774	81->85, 83->86
5	4.7724	259.79	0.0425	82->86
6	4.7871	259	0.0845	83->86, 82->86
7	4.8016	258.21	0.1168	84->86, 81->86
8	5.1292	241.72	0.2289	81->86, 84->86
9	5.2475	236.27	0.0123	79->85
10	5.4056	229.36	0.4202	80->85
11	5.4895	225.86	0.0806	79->86
12	5.5385	223.86	0.2444	80->86, 84->87, 79->86
13	5.6523	219.35	0.0532	84->87, 80->86
14	5.7692	214.91	0.1457	78->85, 83->87
15	5.8028	213.66	0.0039	83->87, 78->85
16	5.9208	209.41	0.0059	81->87, 82->87
17	5.9412	208.68	0.0492	82->87, 81->87
18	6.0196	205.97	0.1641	78->86, 81->87
19	6.3356	195.69	0.0027	84->88, 84->89
20	6.3964	193.83	0.0063	84->89, 83->88, 83->89, 84->88
21	6.4566	192.03	0.0604	80->87
22	6.5204	190.15	0.1262	83->88, 84->88, 83->89, 84->90, 84->89
23	6.5449	189.44	0.0586	83->89, 84->89, 82->88
24	6.563	188.91	0.1631	82->88
25	6.5816	188.38	0.1044	82->89, 82->88, 77->85
26	6.5949	188	0.0026	81->88, 82->89, 76->85
27	6.6112	187.54	0.0188	81->89, 76->85, 81->88
28	6.653	186.36	0.0014	76->85, 81->89, 77->86, 77->85
29	6.7224	184.43	0.0238	77->85, 76->85, 79->87
30	6.7504	183.67	0.0156	79->87

Table 12.3: The first 30 allowed transitions from the ground state of FeCABCN2 (singlet to singlet), calculated with TD-DFT. For each transition, the most important Kohn-Sham molecular orbitals involved are stated.

Excited state	**Energy (eV)**	**Wavelength (nm)**	**Oscillator strength**	**Main molecular orbitals involved**
1	1.9624	631.81	0.0001	209->210, 208->210
2	2.0634	600.88	0	208->210, 206->210, 209->210
3	2.6191	473.38	0.2115	207->210, 209->211
4	2.8269	438.59	0.0002	206->210, 208->210
5	2.938	422	0.0003	208->218, 206->218, 207->211
6	2.9889	414.82	0.0005	208->211, 207->218, 209->212, 206->211
7	3.0109	411.79	0.0085	209->212, 207->218, 209->213
8	3.1265	396.56	0.0157	207->218, 208->211
9	3.1351	395.47	0.3202	209->211, 208->212
10	3.1901	388.65	0.0692	209->213, 209->211
11	3.2233	384.65	0.0101	207->211
12	3.2443	382.15	0.0096	208->213, 208->212, 208->211
13	3.2507	381.41	0.0003	207->212, 209->218, 207->213
14	3.4374	360.69	0.0029	204->210, 207->213, 205->210
15	3.4558	358.77	0	205->210, 207->213
16	3.4808	356.19	0.007	204->210, 207->213, 207->211
17	3.5191	352.32	0.1299	208->212, 209->223
18	3.5295	351.28	0.0368	209->223, 209->218, 208->212
19	3.6249	342.03	0.0007	203->210
20	3.6547	339.24	0.0001	209->218, 203->210, 209->223
21	3.6629	338.48	0.0135	202->210
22	3.7298	332.42	0.0103	206->211, 206->213
23	3.817	324.82	0.0059	206->211, 206->213, 206->212
24	3.8542	321.69	0.0368	206->212, 206->213
25	3.9084	317.22	0.0109	200->210, 201->210, 209->215
26	3.9238	315.98	0.0004	201->210, 200->210
27	3.965	312.7	0.0391	209->215, 209->216
28	4.0713	304.53	0.0002	208->215, 208->216
29	4.1044	302.08	0.0035	208->223, 197->210, 206->223
30	4.1588	298.13	0.0477	208->214